



High-resolution coastal hazard assessment along the French Riviera from co-seismic tsunamis generated in the Ligurian fault system

Fatemeh Nemati¹ · Stephan T. Grilli¹ · Mansour Ioualalen² · Laurie Boschetti² · Christophe Larroque² · Jenny Trevisan²

Received: 23 August 2017 / Accepted: 7 December 2018 / Published online: 15 December 2018
© Springer Nature B.V. 2018

Abstract

The French Riviera is a densely populated and touristic coast. It is also one of the most seismically active areas of the Western Mediterranean. This is evidenced by the M_w 6.7–6.9, 1887 earthquake and tsunami, that was triggered nearshore, rupturing the easternmost 40 km of the 80-km-long Ligurian fault system, which runs parallel to and offshore of the Riviera. Here, coastal hazard from co-seismic tsunamis is assessed along the French and part of the Italian Riviera by simulating three Ligurian earthquake scenarios: (1) the 1887 event offshore Genoa, Italy; (2) a similar event transposed to the westernmost 40-km segment of the fault, offshore Nice, France; and (3) the rupture of the entire 80-km fault, which constitutes an extreme case scenario for the region. Simulations of tsunami propagation and coastal impact are performed by one-way coupling with the Boussinesq model FUNWAVE-TVD, in a series of nested grids, using new high-resolution bathymetric and topographic data. Results obtained in 10-m coastal grids provide the highest resolution predictions to date for this section of the French Riviera of co-seismic tsunami coastal hazard, in terms of inundation, runup, and current velocity. In general, the most impacted areas are bays (near *Cap d'Antibes* and *Cap Ferrat*), due to wave buildup and shoaling within semi-enclosed shallow areas, enhanced by possible resonances. In contrast to earlier work, which was based on coarser resolution grids, the area of Nice harbor is found to be rather well sheltered. It should be noted that uniform fault slip was used in the ruptures and runup estimates could locally be enhanced in case of more complex ruptures, such as segmented and heterogeneous ruptures.

Keywords French Riviera · 1887 earthquake · Tsunami hazard mapping · FUNWAVE-TVD

✉ Stephan T. Grilli
grilli@uri.edu

¹ Department of Ocean Engineering, Graduate School of Oceanography, University of Rhode Island, Sheets Building 215, Narragansett, RI 02882, USA

² Université Côte d'Azur, IRD, CNRS, Observatoire de la Côte d'Azur, Géoazur, Campus CNRS Azur, 250 rue Albert Einstein, CS 10269, 06905 Sophia Antipolis Cedex, France

Fig. 1 **a** Western Mediterranean Sea (WMS), with approximate area of **(b)** in Ligurian Sea marked by a red box (red and yellow stars mark the epicenters of the Zemmouri 2003 and Ligure 1887 events); **b** area of northern Ligurian fault system [marked by red box in **(a)**]; several faults, oblique to the margin direction, can be seen (in red) at the foot of the northern Ligurian continental margin. They are 80 km long and extend from Nice (7°15'E) to Savona (8°30'E). The rupture areas corresponding to scenarios S7, S8 and S11 (Table 4) are marked by blue rectangles, with their centroids identified by stars. The black bullet marks the epicenter of the Ligure 1887 event, and yellow bullets mark those of other dated smaller historical earthquakes

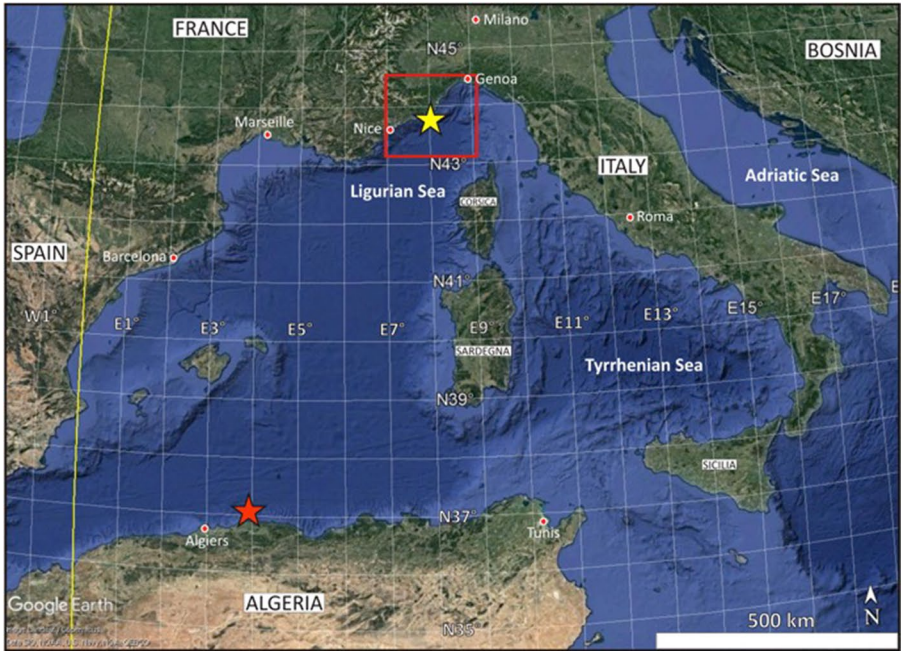
1 Introduction

Historically, the Western Mediterranean Sea (WMS; Fig. 1a) has been regularly affected by large earthquakes that have often triggered significant tsunamis (e.g., Ambraseys 1960; Tinti et al. 2004; Lambert and Terrier 2011; Papadopoulos 2015). In 2003, the $M_w=6.8$ – 6.9 Zemmouri earthquake (Alasset et al. 2006; Heidarzadeh and Satake 2013), sourced near the coast of Algeria (Fig. 1a), triggered the most significant tsunami in recent history in the region, which propagated approximately from south to north in the WMS, causing a 2-m inundation in the Balearic Islands and up to 0.4-m inundation along the French Riviera, from the Spanish to the Italian border. In July 2017, the M_w 6.6 Bodrum–Kos (Turkey–Greece) earthquake triggered the most significant tsunami since this event, causing an up to 1.9-m runup, although little damage occurred (Heidarzadeh et al. 2017).

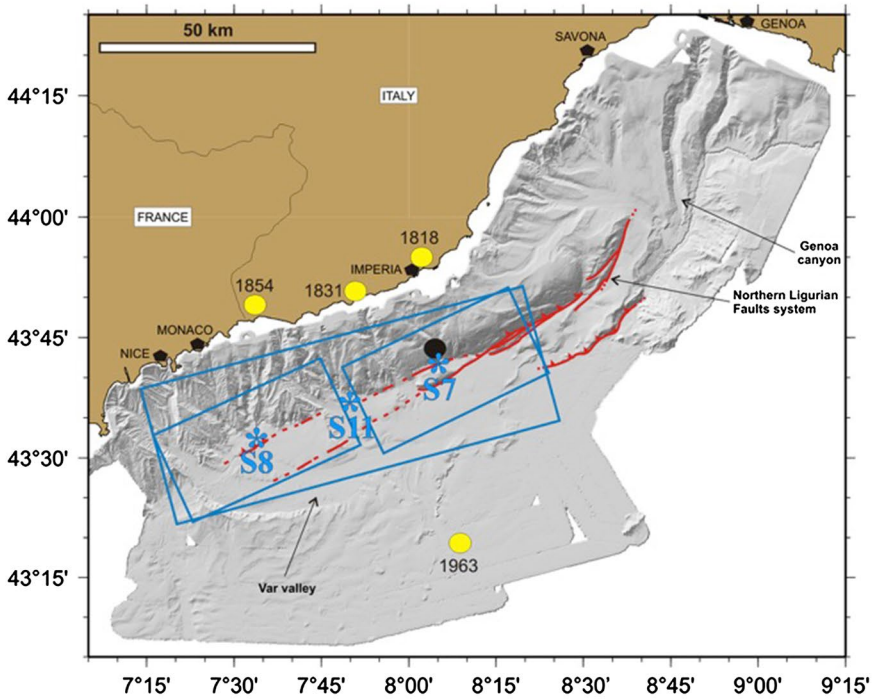
In this work, we perform numerical simulations to assess tsunami hazard along the Ligurian coast, which is located north of the WMS on either side of the French–Italian border (Fig. 1). This is a highly populated coastal area located within one of the most seismically active regions in the WMS, with recurrent earthquakes, onshore and offshore landslides, and frequent tsunamis (Béthoux et al. 1992; Eva et al. 2001; Larroque et al. 2001). During the past 500 years, a dozen tsunamis have been reported to have impacted this area (Tinti et al. 2004; Lambert and Terrier 2011), with most of these having been likely triggered by earthquakes. A notable exception is the October 16, 1979, event (Piper and Savoye 1993; Mulder et al. 1997; Assier-Rzadkiewicz et al. 2000; Ioualalen et al. 2010; Labbé et al. 2012), which was associated with a shallow submarine landslide located on the continental slope, off of Nice’s international airport.

Most of the significant earthquakes that have affected this area have been of moderate magnitude (up to $M_w=5$ or so; Béthoux et al. 1992; Larroque et al. 2009). However, the large $M_w=6.7$ – 6.9 earthquake that occurred on February 23, 1887 (Ferrari 1991; Eva and Rabinovich 1997; Larroque et al. 2012), offshore of Imperia (Italian Riviera) is quite emblematic of future large events that could strike such a low deformation rate area. This earthquake caused 600 fatalities, widespread destruction (Denza 1887; Taramelli and Mercalli 1888), and triggered a tsunami that was observed along more than 200 km of the Ligurian coast; with maximum runups of up to 1–2 m measured from Antibes to Albenga (Fig. 2), this is the most severe co-seismic tsunami observed to date in the northern part of the Western Mediterranean. Simulating this historical event and others similar to it appears essential for assessing tsunami coastal hazard along the Ligurian coast.

Larroque et al. (2012) and Ioualalen et al. (2014) proposed as the likeliest source of the 1887 event (referred to as S7; Fig. 1, Table 4) a shallow rupture scenario (depth 15 km) involving a reverse faulting along a 35-km-long by 17-km-wide segment of the Ligurian faults system (dip 16°N, rake 90°, and strike 55° E). With a 1.3–1.5-m co-seismic slip, the estimated magnitude was $M_w=6.7$ – 6.9 . They performed tsunami generation and



(a)



(b)

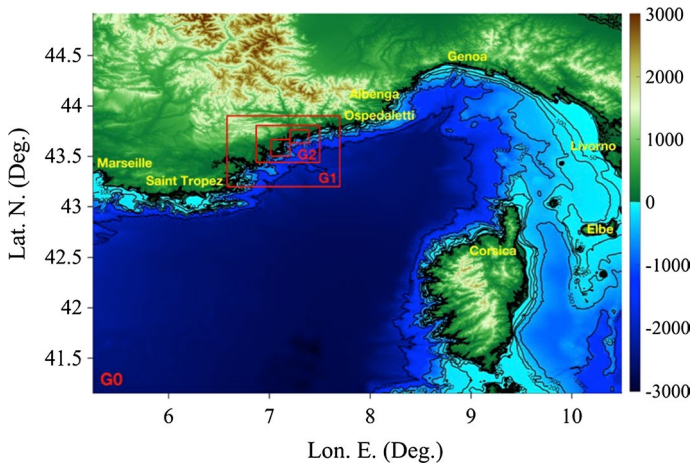


Fig. 2 Footprints of nested computational grids used in this work, referred to as G0–G3a, b (Table 1). Color scale is bathymetry (<0) and topography (>0) of grid G0 in meter. Sponge layers 30 km thick are specified along the offshore boundary of grid G0

propagation simulations on a fairly coarse 100-m resolution grid, which confirmed that for this historical event many localities along the French–Italian Riviera would have experienced significant inundation of up to 2.6 m (flow depth), particularly near Imperia (directly onshore of the co-seismic source). Using the long-wave Boussinesq model FUNWAVE, Ioualalen et al. (2014) studied and modeled other possible rupture scenarios of the Ligurian faults system, covering a wide range of parameters, and simulated the corresponding tsunami coastal impact. In particular, they considered an alternate scenario similar to S7, referred to as S8, with a centroid moved westward, that would occur along the 35-km-long westward segment of the fault. They also parameterized and modeled an extreme scenario of magnitude $M_w = 7.5$, referred to as S11, that would result in the joint activation of all the segments of the 80-km-long Ligurian faults system (with 27 km width and 3.3-m co-seismic slip; Fig. 1 and Table 4). For the latter scenario, simulations predicted a large coastal runup from Nice to Albenga, in the 2–10 m range at most locations, with a very large maximum runup (up to 28 m) within Nice’s harbor and in its immediate vicinity.

Ioualalen et al.’s (2014) results, however, should be put in perspective, first considering the coarse grid resolution (100 m) used in the simulations, which prevented many smaller scale features of the coast, harbors, and marinas from being properly discretized. (For instance, the entrance to Nice’s harbor was only modeled by two grid points.) Such an under-discretization may have caused insufficient damping of incoming tsunami waves, from bottom friction and depth-induced breaking effects, particularly in shallow water regions where depth was rapidly varying. Additionally, tsunami waves may have been trapped and abnormally amplified within harbors whose entrance was insufficiently discretized, causing non-physical enhanced flooding. Second, Ioualalen et al.’s (2014) simulations used a low-resolution shelf bathymetry (their Fig. 1) as well as a similarly rough coastal topography. Combined with the coarse model grid, these bathymetry/topography data did not allow for an adequate representation of coastal protection structures, such as seawalls and piers, that may have otherwise significantly attenuated incident tsunami waves. (This would have particularly affected results in Nice’s harbor.).

Because of the significant risk of a large future event occurring in this region, in this paper, new simulations are performed to better quantify the coastal tsunami hazard posed by the *most realistic scenarios* (S7, S8) and potential *most extreme event* (S11) studied by Ioualalen et al. (2014), using both higher-resolution coastal grids and bathymetry/topography data. Tsunami propagation and coastal impact are simulated using the most recent implementation of the fully nonlinear and dispersive Boussinesq model FUNWAVE-TVD (Shi et al. 2012; Kirby et al. 2013), by one-way coupling, in a series of nested grids of increasingly high resolution toward shore (up to 10 m or so along the coast and onshore). FUNWAVE-TVD's efficient parallel implementation (with more than a 90% scalability) makes it possible efficiently using large high-resolution grids. Besides this capability, FUNWAVE-TVD uses a more accurate moving shoreline algorithm than FUNWAVE, that better captures runup, and has both spherical and Cartesian coordinate grid implementations; the former is important for modeling tsunami propagation in large regional scale domains. Note that in its current implementation, the model's spherical coordinate version is only weakly nonlinear, whereas the Cartesian version is fully nonlinear. Hence, Cartesian grids are used nearshore, which are nested within large-scale spherical coordinate grids; this approach was successfully used in many of our similar earlier works, e.g., Grilli et al. 2013, 2015, 2016 and Tappin et al. 2014. Finally, in this work, besides computing coastal inundation and runup and comparing those to Ioualalen et al.'s (2014), more detailed analyses are performed in critical areas to assess whether resonance could occur in bays and flow velocities could cause navigation hazards.

In the following, we first detail the design of the computational grids, spherical (G0 at about 640-m resolution and G1 at about 160-m resolution) and Cartesian (G2 at 40-m and G3a, b at 10-m resolution), and the bathymetric and topographic data used in those. We then model tsunami generation, propagation, and coastal impact in each grid with FUNWAVE-TVD, for Ioualalen et al.'s (2014) scenarios S7, S8 and S11 and detail and discuss the relevant results.

2 Methodology

2.1 Numerical model

The propagation of co-seismic tsunamis and their coastal impact are modeled in a series of nested grids of increasingly fine resolution toward the coast. Simulations are performed using the fully nonlinear and dispersive Boussinesq model FUNWAVE-TVD. This model is based on the equations of Shi et al. (2012) and is a recent improvement of FUNWAVE (Wei and Kirby 1995; Wei et al. 1995), which was originally developed and used to model nearshore waves, but also applied to a variety of tsunami case studies, both landslide and co-seismic (e.g., Watts et al. 2003; Day et al. 2005; Grilli et al. 2007, 2010, 2013, 2015, 2016, 2017; Ioualalen et al. 2007, 2014; Tappin et al. 2008, 2014; Mård Karlsson et al. 2009; Tehranirad et al. 2015; Shelby et al. 2016; Schambach et al. 2018). FUNWAVE-TVD was fully validated against all of the US National Tsunami Mitigation Program (NTHMP) benchmarks (Tehranirad et al. 2011).

In the more recent of these studies, a one-way nesting methodology was used, which was shown to be sufficiently accurate to perform tsunami coastal hazard assessment case studies (e.g., Grilli et al. 2013; Tappin et al. 2014). This methodology works by running the full duration of simulations in each grid, and computing time series of free surface elevations

and currents in a coarser grid level, at a large number of numerical gages (stations) along the boundary of the next finer grid level. Computations in the finer next nested grid level are then performed using these time series as boundary conditions, re-interpolated over the smaller time step of the finer grid, based on FUNWAVE-TVD's CFL criterion [note, in finer grids, time series are truncated until the time the tsunami reaches this particular grid; see Shi et al. (2012) for detail of the time stepping in FUNWAVE-TVD]. With this approach, reflected waves propagating from inside the area covered by each finer grid are included in the time series computed in the coarser grids along the finer grid boundaries, thus satisfying an open boundary condition.

FUNWAVE-TVD has fully nonlinear Cartesian coordinate (Shi et al. 2012) and weakly nonlinear spherical coordinates (with Coriolis effects; Kirby et al. 2013) implementations. In simulations, spherical grids are typically coarser and used to model larger ocean areas in relatively deeper waters encompassing tsunami sources, whereas Cartesian grids are higher-resolution nested grids used to model tsunami coastal impact. This approach was used, for instance, to model the Tohoku 2011 tsunami, in both the near- and far-field, where the one-way nesting of a combination of spherical and Cartesian grids yielded results in good agreement with field measurements (Grilli et al. 2013; Kirby et al. 2013; Tappin et al. 2014). Both model implementations use a combined finite-volume and finite-difference MUSCL-TVD scheme. Similar to the earlier FUNWAVE version (Wei et al. 1995), improved linear dispersion properties are achieved, up to nearly the deep water limit, by expressing the model equations in terms of the horizontal velocity vector computed at 0.531 times the local depth.

While many landslide tsunamis are dispersive (e.g., Tappin et al. 2008, 2014; Grilli et al. 2015), the importance of dispersive effects in far-field tsunami propagation of co-seismic tsunamis was demonstrated by Ioualalen et al. (2007) for the 2004 Indian Ocean and Grilli et al. (2013) and Kirby et al. (2013) for the 2011 Tohoku, co-seismic tsunamis, by performing the same simulations with or without the dispersive terms in the model equations. Schambach et al. (2018) similarly studied dispersive effects for the near- and far-field propagation of landslide tsunamis. Results showed that, given high enough resolution grids (e.g., 10 m), when using a dispersive model, even long tsunamis that are not initially dispersive and are sourced nearshore, such as considered here, develop undular bores (a.k.a, dispersive shock waves) upon propagating onshore. Such bores, which appear near the crest of N-wave-shaped long waves, are made of shorter waves (hence requiring a fine enough grid to be resolved) that may change both the tsunami elevation and dynamics nearshore (see, e.g., Madsen et al. 2008), and hence tsunami coastal hazard. Without dispersion, these nearshore bores do not appear in model results. Therefore, a dispersive model is preferred in all cases, which automatically allows such phenomena to occur in simulation results when the physics of the considered problem requires it (see Glimsdal et al. 2013, for additional discussions).

Energy dissipation resulting from depth-induced wave breaking is modeled in FUNWAVE-TVD by turning off dispersive terms in the equations when the local elevation to depth ratio exceeds a specified value (typically 0.8). This leads to solving nonlinear shallow water equations (NSWE) for breaking waves, which has been shown to closely approximate their energy dissipation (Shi et al. 2012). In the present simulations, bottom friction dissipation is parameterized as a quadratic term with a friction coefficient C_d based on a Manning coefficient n ; in this case, $C_d = g n^2 / h^{1/3}$, where h denotes the local depth.

FUNWAVE-TVD has a parallel implementation using MPI, allowing to efficiently run it on small or large computer clusters. For the moderate-size grids considered in this paper (see next section; see Table 1 and Fig. 2), with less than 3 million nodes, all simulations

Table 1 Parameters of computational grids used in FUNWAVE-TVD simulations (*M* and *N* are grid sizes along *XY* or lon./lat. directions, respectively)

Grid name	Resolution (arc-s/m)	Geographic extent (lon. E; lat. N)	<i>M</i>	<i>N</i>	Cartesian/spherical	Bathymetry
G0	640 m (lon: 28.08"; lat: 20.88")	(5.23°, 10.5083°); (41.14°, 44.9330°)	676	660	Spherical	GMRT—57-m and 10-m nearshore data
G1	160 m (lon: 7.20"; lat: 5.04")	(6.57°, 7.7117°); (43.2°, 43.9022°)	585	488	Spherical	GMRT—57-m and 10-m nearshore data
G2	40 m	(6.87°, 7.4976°); (43.44°, 43.8065°)	1293	1008	Cartesian	10-m nearshore data
G3a	10 m	(7.015°, 7.2031°); (43.5°, 43.6682°)	1557	1856	Cartesian	10-m nearshore data
G3b	10 m	(7.2031°, 7.39°); (43.63°, 43.7619°)	1557	1456	Cartesian	10-m nearshore data

The GMRT data were obtained from <http://www.marine-geo.org/tools/GMRTMapTool>

were performed in a matter of hours for each grid, using 24 cores on a MacPro Desktop computer (with 64 Gb of RAM).

2.2 Computational grids

Simulations of co-seismic tsunamis in the Ligurian sea (Fig. 1) are performed by one-way coupling in 4 levels of overlapping nested grids: G0–G3a, b (Fig. 2; Table 1). To reduce reflection in the first, coarsest grid, level (here the 640-m Western Mediterranean basin grid G0), 30-km-thick (absorbing) layers are specified along all of the open boundaries (Shi et al. 2012).

Grid resolution is increased by a factor of 4 between each grid levels, from G0–G3a, b, which was shown in earlier work to be sufficient to ensure accurate results (e.g., Grilli et al. 2013; Kirby et al. 2013; Tappin et al. 2014). Specifically, the first two nested grid levels are spherical, with grid G0 having 0.469 by 0.345 arc-min regular meshes in the longitudinal and latitudinal directions, leading to a 640-by-640-m cell resolution, and G1 having 7.038 by 5.180 arc-s regular meshes in the longitudinal and latitudinal directions, leading to a 160-by-160-m resolution. The next two nested grid levels are Cartesian, with grid G2 having 40-by-40-m and G3a, b having 10-by-10-m regular meshes. Figure 2 shows the footprint of each nested computational grid and Table 1 gives their detailed parameters. The coarser grid G0 encompasses a long section of the French and Italian Riviera, from Marseille, France, on the west in the Gulf of Lion, to Piombino, Italy (south of Livorno), in the Gulf of Genoa, with the Corsica and Elbe Islands to the south (Figs. 1, 2). The other (nested) grids G1, G2 and G3a, b are centered on the French Riviera, although grid G1 covers part of the Italian Riviera, beyond Menton, France, where grid G2 ends, to Ospedaletti, Italy (Fig. 2). On the western side, grid G1 starts at the Bay of Saint Tropez–Sainte Maximes, while grid G2 starts at La Beaumette (Figs. 1, 2). The highest resolution grids G3a, b cover the region from Cannes to Saint-Laurent-du-Var, and from Saint-Laurent-du-Var to Cap d’Ail, respectively. Most of these locations and cities are listed in Table 3 and marked in Figs. 3 and 4, which show details of grids G2 and G3a, b.

Several sources of bathymetric–topographic data were used to develop the depth matrices of the various computational grids. When no other higher-resolution data were available, the default datasets were the 57-m resolution GMRT data from <http://www.marine-geo.org/tools/GMRTMapTool> and the nearshore bathymetric and topographic data at 10-m resolution for the French side of the Riviera. The latter dataset was built based on higher-resolution data: the 5-m DTM land topography “GO_06 juin 2009” for the district of the *Alpes Maritimes* (from Cannes to Menton), complemented by the IGN (*Institut National de l’Information Géographique et Forestière*) 50-m grid, over the district, and the 90-m SRTM dataset elsewhere in the computational domain. The nearshore bathymetry resolution was significantly improved using: (1) the Litto3D 5-m grid; and (2) a 2-m grid covering the narrow continental shelf over the *Alpes Maritimes*, obtained from CANCA (*Communauté d’Agglomération de Nice Côte d’Azur*). These data, along with the 5-m DTM land topography, allowed more accurately representing maritime structures (piers and seawalls) than in earlier work. These nearshore bathymetry data were complemented in deeper water by a 25-m grid dataset built from multi-beam surveys carried out during numerous cruises: CALMAR, DELTARHO1.LEG1, DELTARHO1.LEG2, DELTARHO2, PROFANS3, ESS300/1, MATOU1, MATOU2, MESEA I, MESIM.LEG1 (MESEA 2), MESIM.LEG2 (MESEA 2), SEADOME,

TRANSRHO, MALISAR1, GMO, MALISAR2, MALISAR3. The 20-to-200-m bathymetric contours of UNESCO IOC-IBCM (*Intergovernmental Oceanographic Commission—International Bathymetric Chart of the Mediterranean*) complemented the dataset, which is of particular interest along the Italian border, once merged with the GMRT dataset. The interpolated bathymetry/topography of grids G0, G1 and G2 are shown in Figs. 2, 3, and 4.

Bottom friction is specified in simulations through the Manning n coefficient value. Tehranirad et al. (2015) showed that, on a wide shelf (such as along the US East Coast), using even a moderate bottom friction with $n=0.025$ (the value for coarse sand) causes a significant gradual reduction in incident tsunami waves. Schambach et al. (2018) further showed that, using higher values of n in finer resolution nearshore grids (e.g., 0.0375) led to a significant reduction in maximum tsunami inundation. Hence, for tsunami hazard assessment and in the absence of more detailed information on land use, they recommended using the conservative $n=0.025$ value for coarse sand. In the present simulations, considering the French Riviera has a coastline mostly fronted by coarse sand/small pebble beaches, this value is used in each grid. Additionally, to prevent abnormally large friction coefficient values onshore, a minimum depth was specified, below which the friction coefficient was kept constant. In the coarser grids G0 and G1, this minimum depth is set to 2 m, which yields, $C_d=0.0013$ to 0.0049 when depth h varies from 100 to 2 m (note the standard value for coarse sand is $C_d=0.0025$); hence, bottom friction should only cause a moderate dissipation of incoming tsunami waves in deep water, and particularly more so considering the narrow continental shelf in this area (see Figs. 2, 3, and 4), which is conservative. In the finer resolution grids G2 and G3a, b, in which tsunami coastal impact is more accurately computed in terms of maximum inundation and runup, the minimum depth is set to 1 m and 0.5 m, respectively, which yields maximum values for the friction coefficient of $C_d=0.0061$ and 0.0077, respectively; these are still moderate friction coefficients in view of the significant development of the coastline and, hence, are also conservative values as far as predicting maximum flow depth at the coastline.

Stations/numerical gages are specified in all nested grids, to both verify that results of nested simulations are consistent with each other in the various grids and compute time series of tsunami elevation at locations of specific interest (e.g., inside harbors to assess resonance). Table 2 shows lat–lon coordinates, depth, and label of stations specified in grids G0–G3a, and Figs. 3, 4, and 5a show locations of these stations in the various grids.

Table 2 Geographic location, depth, and existence in various nested grids (0 or 1) of stations/numerical wave gages used to validate nested grid simulations

No.	Lon. (°E)	Lat. (°N)	Depth (m)	G0	G1	G2	G3a
1	7.651	43.72	725.53	1	1	0	0
2	7.537	43.70	591.18	1	1	0	0
3	7.435	43.29	2251.5	1	1	0	0
4	7.013	43.28	1398.3	1	1	0	0
5	7.474	43.55	1890.3	1	1	1	0
6	7.279	43.45	1685.3	1	1	1	0
7	7.013	43.449	965.27	1	1	1	0
8	7.129	43.5701	6.72	1	1	1	1
9	7.162	43.58	94.98	1	1	1	1

2.3 Co-seismic tsunami sources

Tsunami generation and propagation are modeled for three shallow seismic sources originating within the Ligurian fault system (Table 4; Ioualalen et al. 2014), referred to as: (1) S7, a M_w 6.9 rupture of the eastern segment of the fault, approximately corresponding to the 1887 rupture, such as estimated by Ioualalen et al. (2014); (2) S8, which has similar parameters, but with its centroid shifted westward on the fault offshore of Nice; and (3) S11, an extreme (for this area) M_w 7.5 rupture of the entire 80-km-long fault, for which some of the parameters were deduced from the seismic scaling laws proposed by Wells and Coppersmith (1994).

Ioualalen et al.'s (2014) best-fit solution for the 1887 event source (S7) was selected among an ensemble of numerical simulations as that which agreed best with the tide gauge time series recorded in Genoa harbor (Italy). This solution corresponds to a 35-km-long rupture located on the eastern side of the 80-km-long Ligurian faults system (Fig. 1). Regarding the extreme M_w 7.5 S11 source, although there is no historical record of such a magnitude event ever occurring, the geology and local faulting make it realistic considering such a scenario, which would be mobilizing the entire fault, even though its return period is unknown and could possibly be multi-centennial. In the absence of historical data on extreme seismic sources, however, it is customary in tsunami hazard assessment to assume an extreme scenario that mobilizes the full length of a fault (see, e.g., Grilli et al. 2010), using the maximum slip value that has been observed either at the same or at a nearby location or can be inferred from scaling laws (Wells and Coppersmith 1994). This is the approach pursued for tsunami hazard assessment and inundation mapping performed along the US East Coast for NTHMP.

The seafloor deformation caused by each co-seismic source is computed using the standard Okada (1985) method, based on the parameters listed in Table 4. This method assumes a dislocation of slip S within a rectangular fault area (L , W), in an homogeneous half space whose material has a Coulomb modulus μ (here selected at 3.3×10^{10} Pa); the fault plane has an azimuth θ and is dipping with angle δ ; the slip vector is in rake direction ρ . As is standard in co-seismic tsunami simulations, this deformation is specified at time $t=0$ on the free surface, as an initial condition in the propagation model (FUNWAVE-TVD), with a zero initial flow velocity.

Figure 5 shows the initial tsunami surface elevations computed for the S7, S8 and S11 ruptures, which are specified as initial condition in grid G0. Because these initial sources overlap with the nested grids, whose footprints are marked on the figure, the initial surface elevations of tsunami sources were re-interpolated onto those grids and used as initial conditions together with the time series computed in the coarser grid levels specified as boundary conditions. For sources S7 and S8, which have the same parameters and magnitude, Fig. 5a, b shows a minimum surface elevation of -0.12 m and a maximum surface elevation of 0.31 m, whereas for the larger and stronger S11 source, these are -0.41 m and 1.01 m, respectively, in Fig. 5c.

Table 3 Location of key coastal sites used in runup calculations, in nested grids simulations, belonging to G2 or G3a, b grids, with their resolution (marked in Figs. 3 and 4)

Site no.	Site name	Grid no.	Resolution (m)
1	Iles de Lérins (islands offshore Cannes)	G3a	10
2	Cape d’Antibes/plage de la Salis	G3a	10
3	Saint-Laurent-du-Var	G3a	10
4	Nice international airport	G3b	10
5	Nice Massena (Nice harbor area)	G3b	10
6	Villefranche-sur-Mer	G3b	10
7	Saint-Jean Cap Ferrat	G3b	10
8	Monaco	G2	40
9	Rocquebrune Cap Martin	G2	40
10	Menton	G2	40

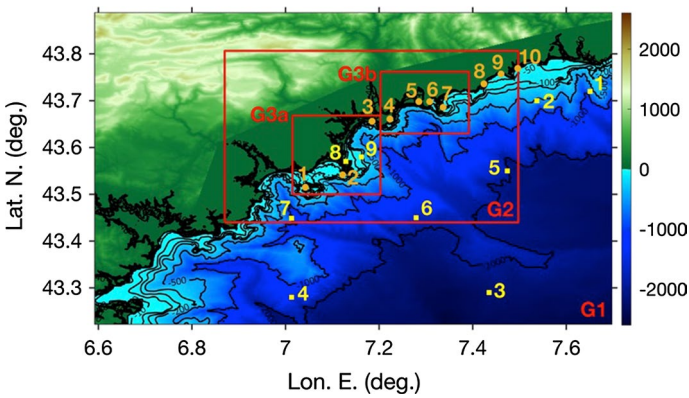


Fig. 3 Footprints of nested computational grids G1–G3a, b (Table 1). Color scale is bathymetry (<math><0</math>) and topography (>0) of grid G1 in meter; black lines are bathymetric contours. Numbered symbols mark locations of wave gage stations (yellow squares; Tables 2) and key coastal sites (brown bullets; Table 3)

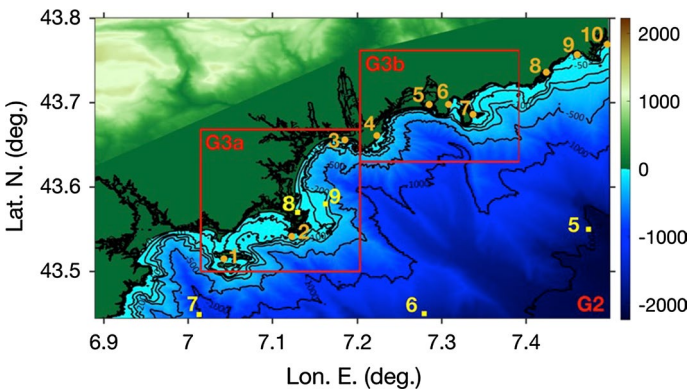


Fig. 4 Same as Fig. 3 for grids G2 and G3a, b (Table 1)

Fig. 5 Co-seismic tsunami source elevation (color scale in meter) computed using Okada's method in grid G0 for the: **a** S7, M_w 6.9; **b** S8, M_w 6.9; and **c** S11, M_w 7.5, Ligurian events (Table 4). Footprints of nested grids G1, G2, G3a, b are marked by red boxes (Figs. 3, 4). Note the different color scales used in each sub-figure

3 Simulation results

For each of the seismic sources S7, S8 and S11 (Table 4) shown in Fig. 5, simulations with FUNWAVE-TVD are performed by one-way coupling in the series of nested grids G0–G3a, b (Table 1; Figs. 2 and 3). Among many model results, the time series computed at stations specified in each grid (Tables 2; Figs. 2, 3, and 4) and the envelope of maximum surface elevations during computations are detailed in the following; additionally, some envelopes of maximum flow velocity are discussed. Simulations are performed for 1.5-h (5400-s) duration, to ensure that all waves resulting from multiple reflections in the Mediterranean basin have arrived.

3.1 Tsunami surface elevations and inundation

Figure 6 shows envelopes of maximum surface elevations computed in grids G1 and G2 for each source. Consistent with each source location and magnitude, the tsunami surface elevations simulated at the coast are larger for source S11 than for sources (S7, S8) and also larger for the source closest to the coast. These results also show, as could be expected, that coastal surface elevations are larger within small bays/enclosures and harbors/marinas due to the buildup and possible resonances of trapped waves. This is better seen in results of simulations in the finer grids G3a, b detailed later.

To both visualize the incident tsunami wave train and verify that the one-way coupling method has been properly applied to grids G0–G3, Fig. 7 shows time series of surface elevations computed for source S7 at control stations 1–9 (Figs. 3, 4; Table 4). For stations 1 to 4, time series of surface elevations obtained at the same location in nested grids G0 and G1 are compared with each other, and for stations 5 to 9, time series of surface elevations obtained at the same location in nested grids G0, G1 and G2 are compared. At stations 8 and 9, which are located near Antibes, time series of surface elevations obtained in nested grids G0, G1, G2 and G3a are compared.

Overall, these figures show a good agreement of time series computed in various grids, particularly for the incident part of each wave train (i.e., for $t < 0.25$ h or 15 min or so), except at the nearshore station 8. As waves are partially reflected from the shore and travel back to the stations, discrepancies become larger later in time between results obtained in grids of different resolution, and this is particularly so at station 8; this should be expected since grid resolution affects tsunami–shore interactions.

These results confirm the accuracy of the nested simulations in grids G0–G2 (G3a). Also note that, as should also be expected, the amplitude of the incident tsunami at stations 1, 2, 8 and 9 nearer the coast is larger than at the offshore stations. Similarly consistent results were obtained at stations belonging to different nested grids for sources S8 and S11; details are not shown here for the sake of brevity.

Figure 8 shows envelopes of maximum surface elevations computed in grids G3a, b for each source S7, S8, and S11, and Figs. 9, 10, 11, 12, 13, 14, and 15 show zoom-ins of these results around seven regions of particular impact or importance, located in grids G3a,

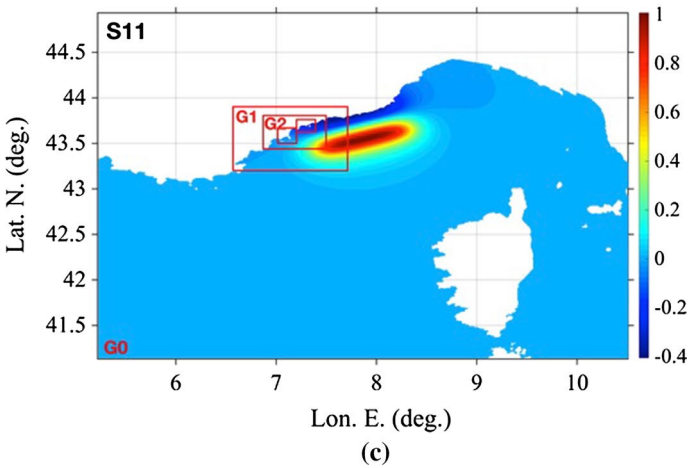
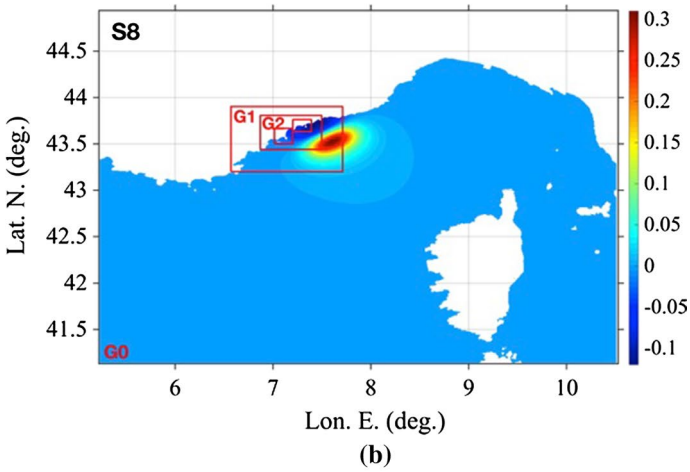
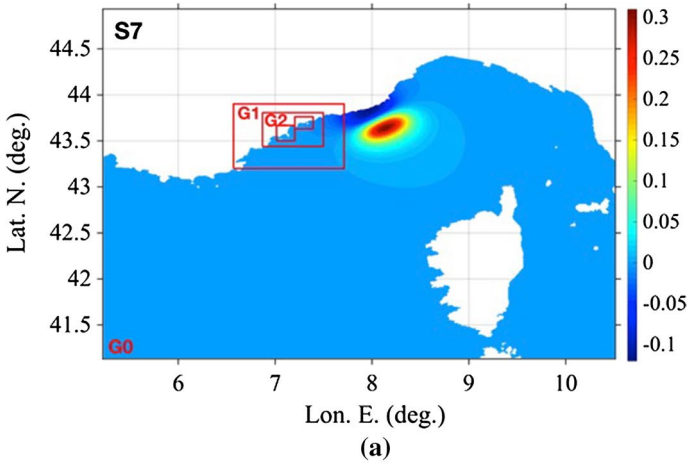


Table 4 Parameters of Okada's (1985) method for computing the three Ligurian fault co-seismic tsunami sources used in FUNWAVE-TVD simulations (Fig. 5): (i) centroid geographic coordinates (ϕ_0 , λ_0); (ii) rupture depth d ; (iii) azimuth θ (CW from N); (iv) dip δ ; (v) rake ρ ; (vi) length and width (L , W); (vii) slip S ; (viii) magnitude $M_w = (\log M_0 - 9.1)/1.5$ ($M_0 = \mu LWS$; $\mu = 3.3 \times 10^{10}$ Pa)

Source	ϕ_0 ($^{\circ}$ N)	λ_0 ($^{\circ}$ E)	d (km)	θ	δ	ρ	L (km)	W (km)	S (m)	M_w
S7	43.7	8.08	15	235	16	90	35	17	1.5	6.91
S8	43.58	7.55	15	235	16	90	35	17	1.5	6.91
S11	43.64	7.815	15	250	16	90	80	27	3.3	7.51

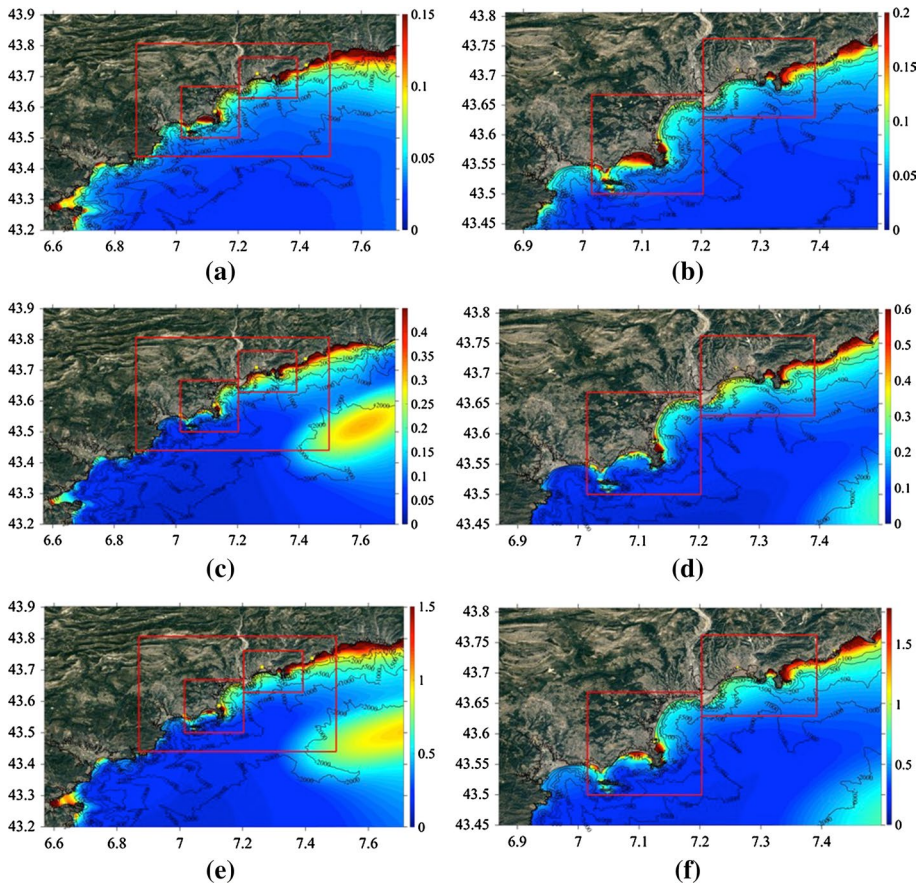


Fig. 6 Envelope of maximum surface elevation (color scale in meter) computed in grids: (left) G1, and (right) G2, during tsunami simulations of sources S7 (a, b), S8 (c, d), and S11 (e, f). Red lines mark footprints of finer nested grids defined before (Fig. 5). Yellow squares mark the sites of Cannes, Antibes, Nice, Monaco-Ville, and San Remo cities, sequentially from left to right (also see Fig. 3 and Table 3). Note the different color scales used in each subfigure

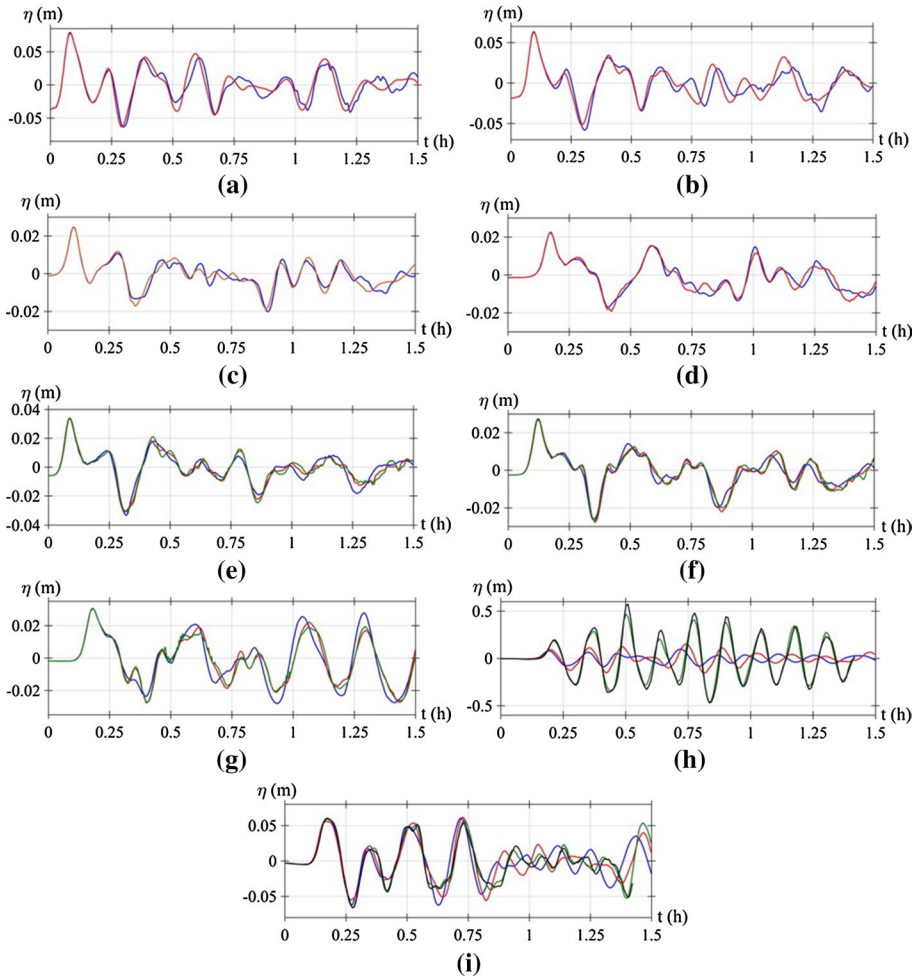


Fig. 7 Comparison of time series of surface elevations computed for source S7 in grids G0 (red), G1 (blue), G2 (green), and G3a (black) at stations No.: **a** 1; **b** 2, **c** 3; **d** 4; **e** 5; **f** 6; **g** 7; **h** 8; **i** 9 (Figs. 3, 4, Table 4). Note, surface elevations at station No. 8, which is nearshore, are ten times larger than at other stations

b, namely from west to east (see Fig. 4 and Table 3): (1) Ile Sainte-Marguerite; (2) Port Palm Beach; (3) Cap d’Antibes; (4) Port of Nice; (5) Rade de Villefranche-Sur-Mer; (6) St Jean Cap Ferrat; (7) Port of Beaulieu-sur-Mer. Overall, as would be expected, we find that the tsunami coastal inundation caused by source S11 is larger at every location than that caused by the two other smaller-size sources S7 and S8 and by more than a factor of 2 at most locations, with maximum runup reaching over 2.0, 2.0, 3.5, 1.5, 2.0, 3.0, and 5.0 m in each of the seven zoomed-in areas, respectively. It should be noted that many of these locations of maximum inundation are within small bays or marinas, where amplification and possibly resonance may have occurred. In such locations, it is expected that large current velocities would be associated with even moderate surface elevations, due to funneling effects, which could end up being more damaging for moored boats and harbor facilities

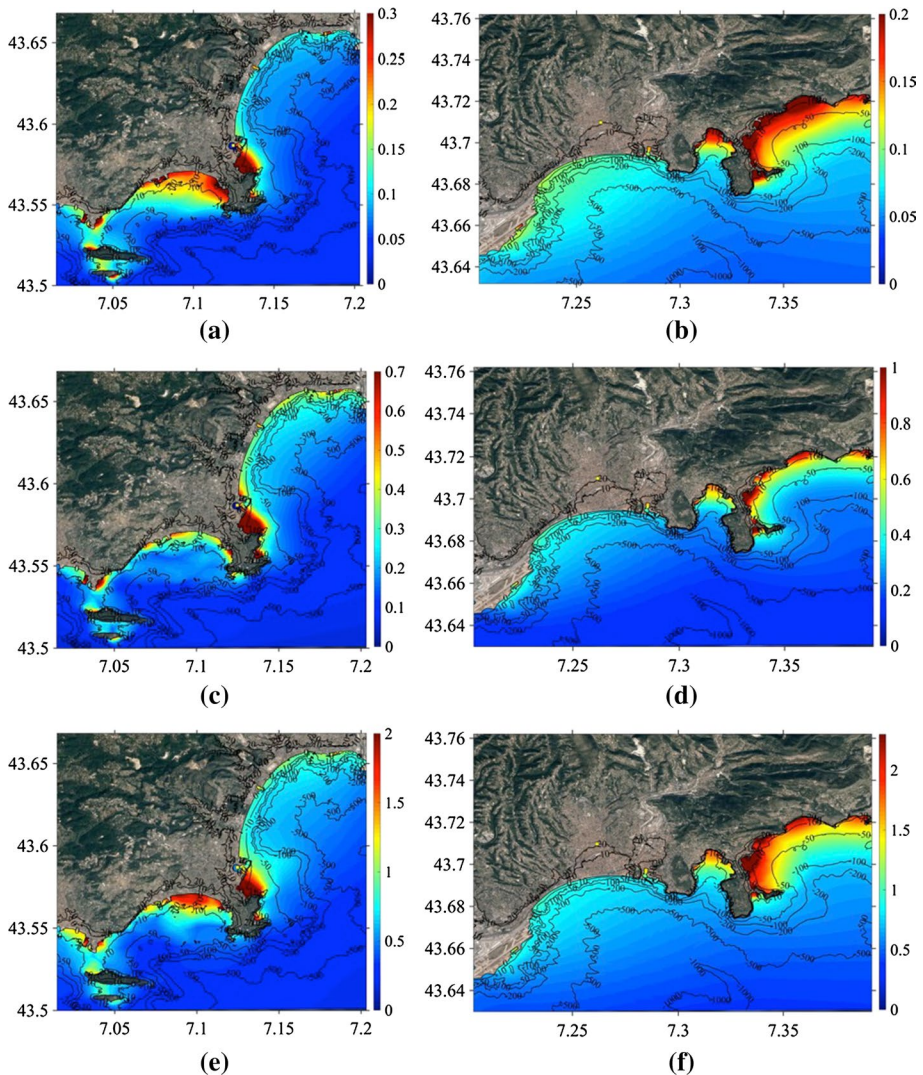


Fig. 8 Envelope of maximum surface elevation (color scale in meter) computed in grids: (left) G3a and (right) G3b during tsunami simulations of sources S7 (a, b), S8 (c, d), and S11 (e, f). Note the different color scales used in each subfigure

than the inundation itself. Both of these aspects are detailed later in the text (Sects. 3.3 and 3.4).

Other sites where the largest tsunami inundation occurs for all sources are capes, such as *Cap d'Antibes* (Fig. 11) and *Saint-Jean Cap Ferrat* (Fig. 14). Here, typically the isobaths are concave shaped (referred to land) causing tsunami wave and energy focusing due to refraction. *Cap de Nice* (known as *Baie des Anges*) is an exception with the isobaths being convexly oriented (see, for instance, the 500-m isobaths in Fig. 8b, d, f), allowing for a slight wave damping due to wave divergence.

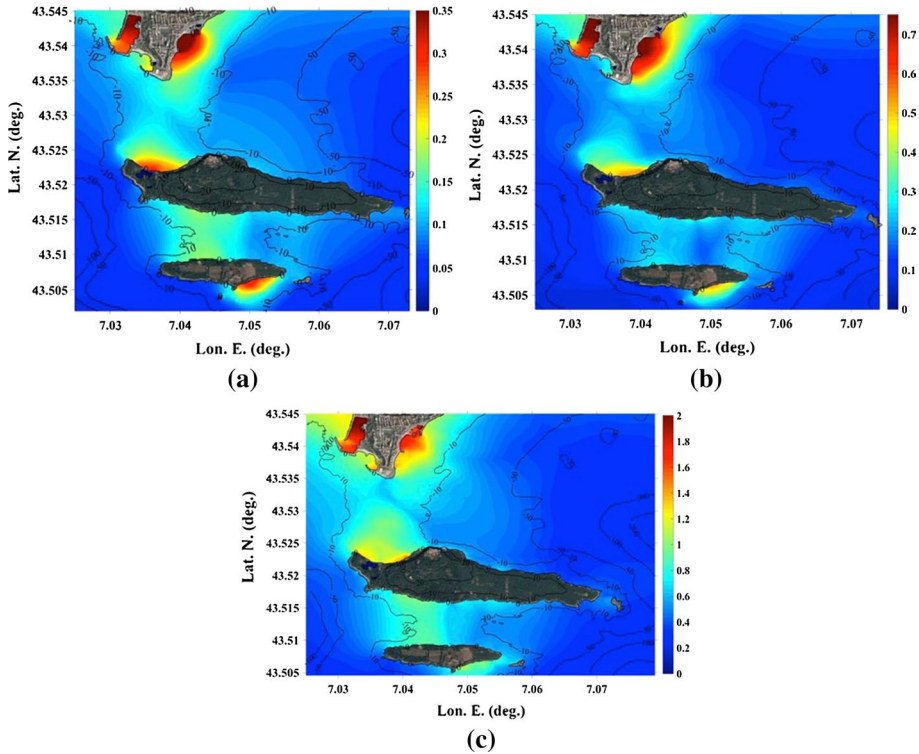


Fig. 9 Zoom-ins of Fig. 8a, c, e around Ile Sainte-Marguerite (Fig. 4 and Table 3) for sources: **a** S7, **b** S8, **c** S11. Note the different color scales used in each subfigure

Similarly, the two large open bays located between Antibes and Nice Airport and eastward of *Cap de Nice* also feature convex-type isobaths, which generate some wave damping that compensates for some of the wave amplification due to shoaling (Fig. 8). These two large bays are thus rather sheltered with respect to tsunami threat. These are densely populated areas during the summer season (including on beaches). Note that Ioualalen et al. (2010) found the same trends of wave focusing–defocusing for cases of landslides-generated tsunamis off of the Ligurian coast. This illustrates and confirms the strong bathymetric control on tsunami coastal impact.

Although the higher-resolution grids G3a, b do not reach that far, the maximum tsunami inundation caused by the extreme source S11 can be quantified east of grid G3b’s area based on simulation results in grids G1 and G2. This is detailed in Fig. 16, which zooms-in on results of Fig. 6e in grid G1 and Fig. 6f in grid G2. This yields the following maximum inundations at various sites of interest: (1) Cap d’Ail, 1.8 m; (2) Monaco, 2.3–2.5 m; (3) Roquebrune-Cap-Martin, 3.5 m; (4) Menton, 3 m; (5) Ponte San Ludovico, 2.5 m; (6) Latte, 3 m; (7) Ventimiglia, 2.5 m; (8) Vallecrosia, 1.8 m; and (9) Ospedaletti, 2 m.

Similarly, west of grid G2, Fig. 17 shows a zoom-in on the area of increased tsunami inundation, up to 2 m, in the bay of Saint Tropez and Sainte Maxime.

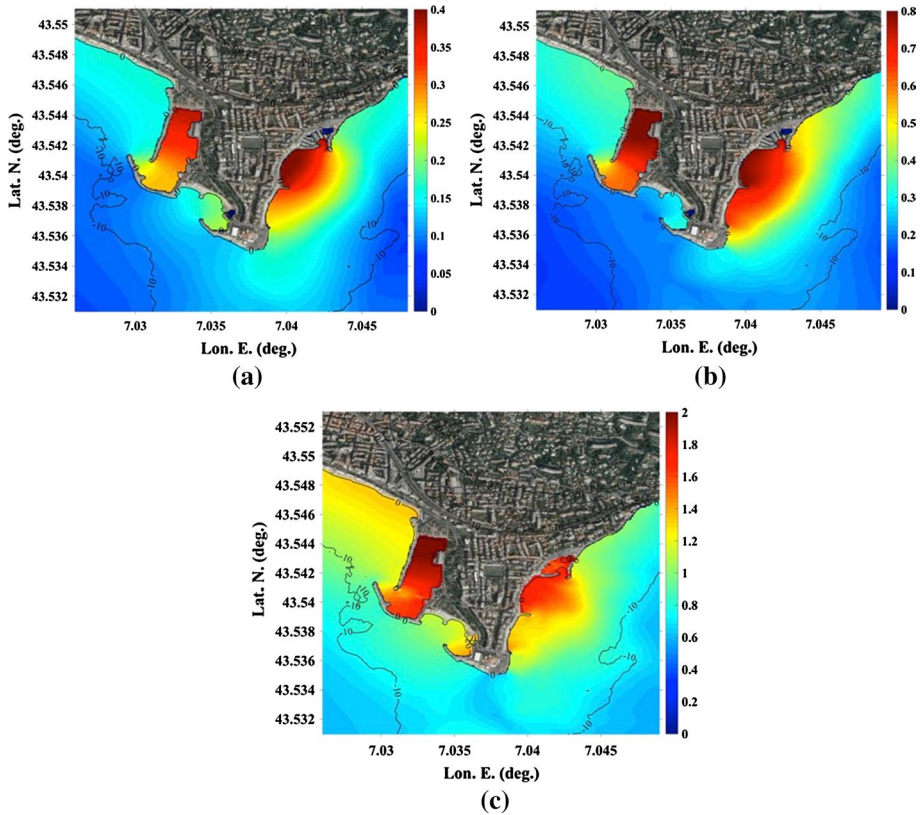


Fig. 10 Zoom-ins of Fig. 8a, c, e around Port Palm Beach and Pointe Croisette (Fig. 4 and Table 3) for sources: **a** S7, **b** S8, **c** S11. Note Cannes' beach is directly to the west of the figure area. Note the different color scales used in each subfigure

3.2 Runup

Figure 18 shows the maximum runup computed for each source along the French Riviera, from Lerin's Island to Saint-Jean Cap Ferrat (sites numbered 1–7; Table 3, Figs. 3, 4), in the 10-m grids G3a, b. Earlier tsunami hazard assessment work performed with FUNWAVE-TVD along the US East Coast (e.g., Grilli et al. 2015; Schambach et al. 2018) indicated that at least 30-m resolution coastal grids, or preferably 10 m, should be used for tsunami inundation/runup results to converge; this is also the recommendation of the US NTHMP. Accordingly, for the purpose of coastal tsunami hazard assessment, in the present study, recommendations should be drawn based on runups computed in the 10-m grids. However, for comparison, results obtained with FUNWAVE-TVD in the 40-m grid G2 are also shown in Fig. 18. Results obtained with FUNWAVE-TVD are also compared in the figure to those of Ioualalen et al. (2014) (hereafter referred to as ILSD14), obtained with FUNWAVE in a coarse 100-m resolution grid, using the coarser and less accurate bathymetry/topography data available at the time. Since the main motivation for the present work was to redo ILSD14's study using higher-resolution grids and bathymetry/topography data, it is important to perform this comparison. Finally, to assess convergence and

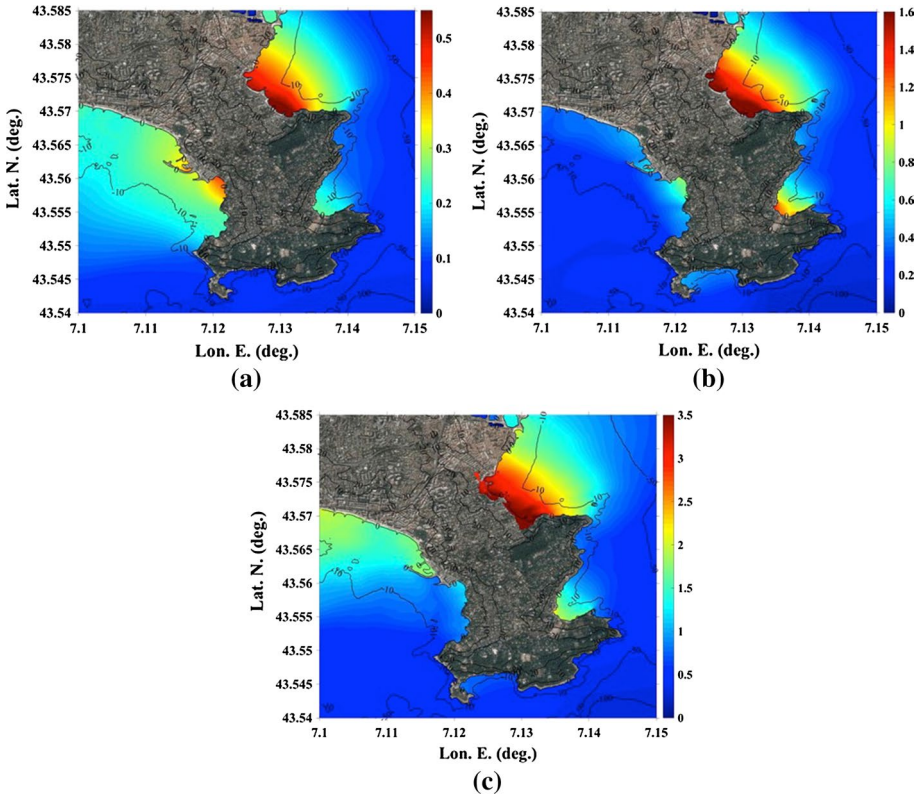


Fig. 11 Zoom-ins of Fig. 8a, c, e around Cap d’Antibes for sources: **a** S7, **b** S8, **c** S11. Note Juan les Pins is to the west and Antibes and its port to the east of the figure area (Fig. 4 and Table 3). Note the different color scales used in each subfigure

better compare model results with each other, a newer set of simulations was performed with FUNWAVE, in a single large 40-m resolution grid encompassing the three sources, using the same new bathymetric/topographic data as used in the FUNWAVE-TVD simulations; runups computed in the latter results are also marked in Fig. 18. Note that although runups were available eastward of Saint-Jean Cap Ferrat and along the Italian coast in the present simulations with FUNWAVE-TVD, this was only in grids G0–G2, which based on our experience and the NTHMP guidelines may have insufficient resolution to accurately capture the runup; hence, these results are not shown in Fig. 18, although overall inundations computed in grids G1 and G2 are shown in Fig. 6.

In summary, based on results displayed in Fig. 18, the following comparisons can be made, which are discussed in the following, for results of: (1) FUNWAVE-TVD 10 m versus 40 m (same model and bathymetry/topography data, but different resolutions); (2) FUNWAVE 100 m versus 40 m (same model but different resolution and bathymetry/topography data), in light of the 10 m FUNWAVE-TVD results; and, (3) FUNWAVE 40 m versus FUNWAVE-TVD 40 m (different models with same resolution and same bathymetry/topography data).

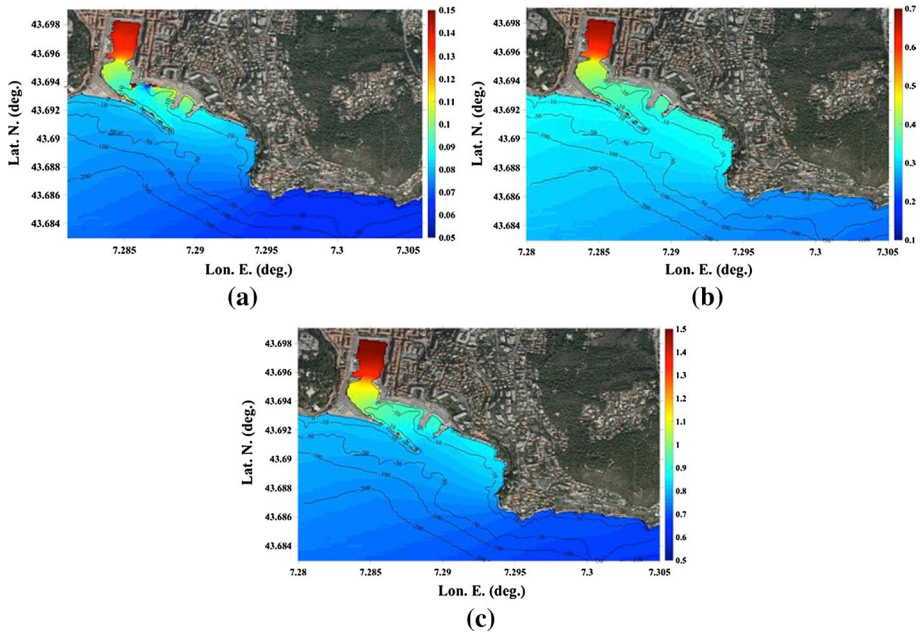


Fig. 12 Zoom-ins of Fig. 8b, d, f around Nice’s harbor (Fig. 4 and Table 3) for sources: **a** S7, **b** S8, **c** S11. Note the different color scales used in each subfigure

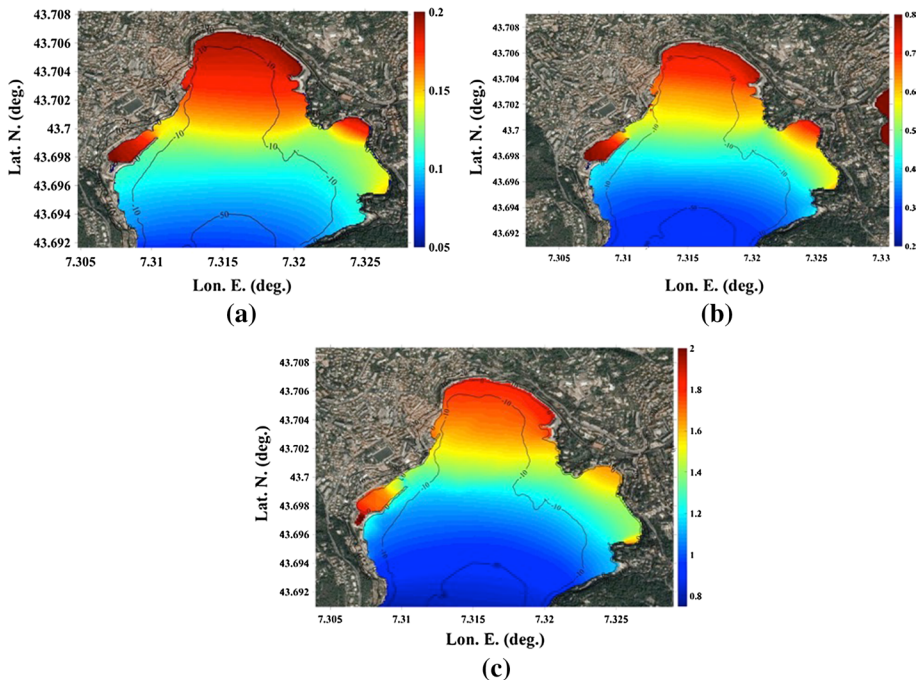


Fig. 13 Zoom-ins of Fig. 8b, d, f around Rade de Villefranche-Sur-Mer (Fig. 4 and Table 3) for sources: **a** S7, **b** S8, **c** S11. Note the different color scales used in each subfigure

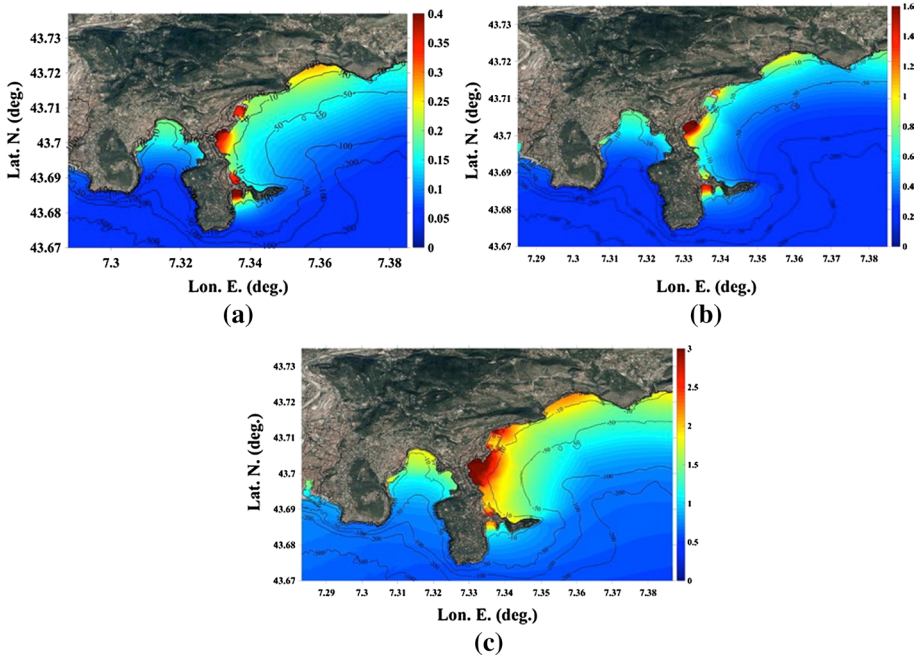


Fig. 14 Zoom-ins of Fig. 8b, d, f around St Jean Cap Ferrat and its harbor for sources: **a** S7, **b** S8, **c** S11. Note the harbor of Beaulieu-sur-Mer (detailed in the next figure) is north of the cape (Fig. 4 and Table 3). Note the different color scales used in each subfigure

1. Overall, for all sources, runups in Fig. 18 computed with FUNWAVE-TVD in the 40-m and 10-m resolution grids appear consistent with each other, indicating that convergence of these simulations may have been achieved. This is further supported by the mean and standard deviation of computed runups listed in Tables 5, 6, and 7, which for all sources are very similar in these two grids. The root-mean-square-difference (RMSD) of the 40-m simulation results with respect to the 10-m results is satisfactory, ranging from 4 to 25% for all sources. Likewise, the determination coefficient is relatively close to unity (0.81, 0.68 and 0.88 for S7, S8 and S11, respectively), and the L^2 norm is also satisfactory as it is relatively small (0.23, 0.33 and 0.18 for S7, S8 and S11, respectively). The cross-correlation coefficient between results in both grids is very good, always larger than 0.8. Therefore, in either grid, runups computed with FUNWAVE-TVD appear to be adequate although based on standard recommendations (e.g., NTHMP) 10-m results should be preferred to draw conclusions.
2. Comparing the present simulations to those of ILSD14 with FUNWAVE in a coarse 100-m grid, Fig. 18 shows significant differences, with the latter often significantly over-predicting or slightly under-predicting runups. This confirms that both the grid and likely also the bathymetry/topography data used in the earlier work were insufficiently discretized; nearshore and along the entire coast, bathymetric and topographic data used by ILSD14 were sparse. As discussed before, the under-resolving of coastal features likely led in some cases to insufficient nearshore dissipation or wave trapping that artificially increased runup; this explains the very large 28-m runup predicted by ILSD14 for source S11 in Nice’s harbor (site 5 in Fig. 18c; this single large value was

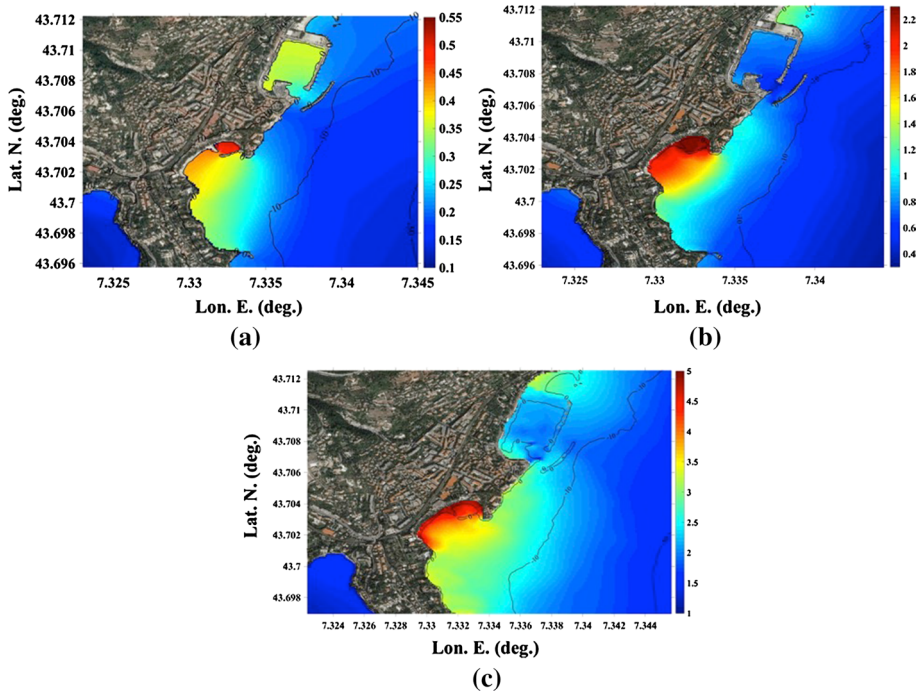


Fig. 15 Zoom-ins of Fig. 7b, d, f around Beaulieu-sur-Mer's harbor (Fig. 4 and Table 3) for sources: **a** S7, **b** S8, **c** S11. Note the different color scales used in each subfigure

omitted from the figure for clarity), which should be deemed spurious. The poor values of the detailed metrics in Tables 5, 6, and 7 (R^2 , L^2 , Corr) support this conclusion.

By contrast, the new 40-m resolution simulations with FUNWAVE, using the new more accurate bathymetry/topography data, provide significantly different runup values in Fig. 18, as compared to the 100-m results, that are in much better agreement with the present higher-resolution simulations with FUNWAVE-TVD; these also no longer predict the spurious large runup in Nice's harbor. This is also confirmed by the good values of the metrics in Tables 5, 6, and 7. The convergence of FUNWAVE's results with increasing resolution is reassuring.

3. The comparison of runups simulated with FUNWAVE-TVD and FUNWAVE in the 40-m resolution grid, based on the same bathymetry/topography data, shows a good overall agreement in Fig. 18. Larger differences occur mostly where runups are the largest, with FUNWAVE's results being slightly above those of FUNWAVE-TVD. This is consistent with the new moving shoreline algorithm that was implemented in FUNWAVE-TVD, to replace the simple slot method used in FUNWAVE, following a careful validation based on laboratory experiments (Shi et al. 2012).

3.3 Local bay resonance

Two sites are of particular interest in Fig. 18 results: Cap d'Antibes—Plage de la Salis (site 2) and Saint-Jean Cap Ferrat (site 7). Both of these are semi-enclosed bays where, for

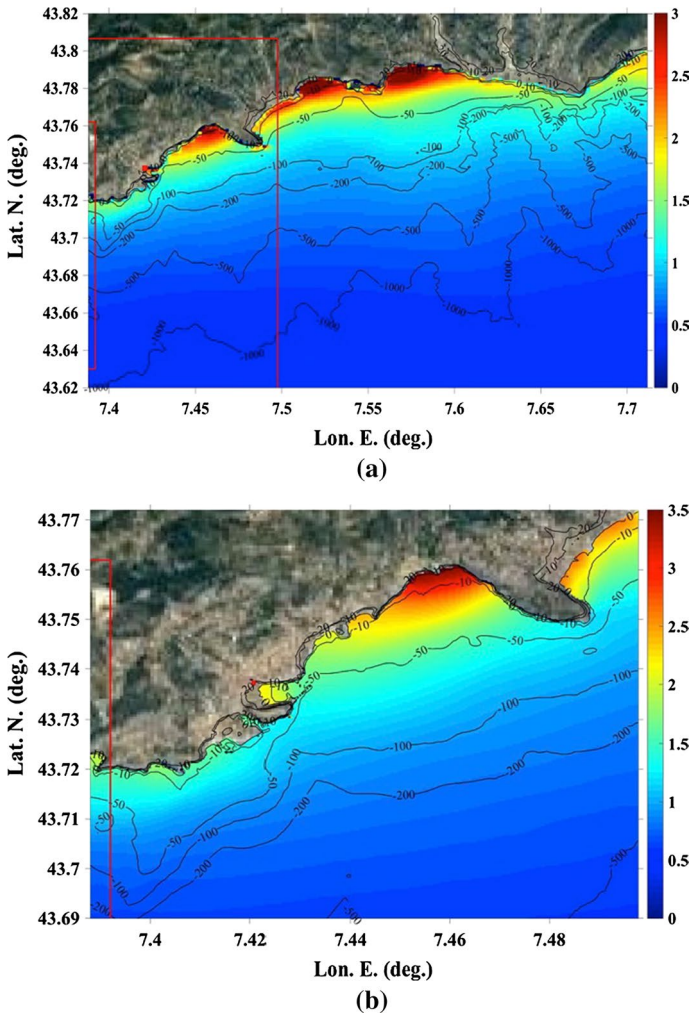


Fig. 16 Zoom-ins of maximum surface elevations (color scales in meter) computed for source S11 in grids: **a** G1 (Fig. 6e), and **b** G2 (Fig. 6f). For reference, the longitude of important areas is (maximum elevation is in parenthesis): (i) Cap d’Ail, 7.41 (1.8 m); (ii) Monaco, 7.425 (2.3–2.5 m); (iii) Roquebrune-Cap-Martin, 7.475 (3.5 m); (iv) Menton, 7.498 (3 m); (v) Ponte San Ludovico, 7.537 (2.5 m); (vi) Latte, 7.570 (3 m); (vii) Ventimiglia, 7.608 (2.5 m); (viii) Vallecrosia, 7.645 (1.8 m); and (ix) Ospedaletti, 7.712 (2 m) [locations (i–iv) are in France and the others in Italy]. Red lines mark the boundaries of nested grids. Also see Figs. 3, 4 and Table 3 for site locations. Note the different color scales used in each subfigure

the three sources, tsunami runup is enhanced as compared to neighboring sites. A more detailed analysis of this phenomenon was performed for site 2, where some of the largest runup values are predicted for all sources in the 10-m grids. Figure 19 shows time series of surface elevations computed at site 2, at two wave gage/stations, one located just within the bay (station 8, Fig. 4) and one outside of it (station 9, Fig. 4; see also results in Fig. 11).

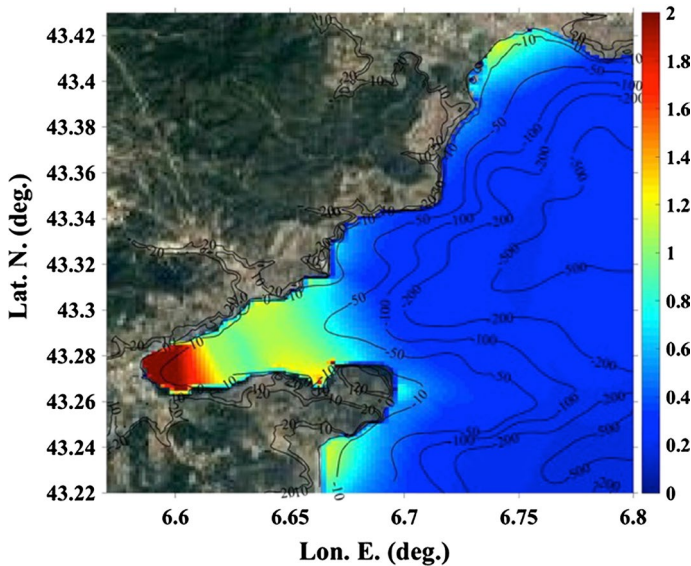


Fig. 17 Zoom-in of maximum surface elevations (color scales in meter) computed for source S11 in grid G1 (Fig. 6e), in the area of Saint Tropez and Sainte Maxime (enclosed bay to the SW; Fig. 4 and Table 3)

The figure shows that, for all sources, the incoming wave time series are amplified within the bay, by a factor larger than 2.5.

The depth amplification factor based on linear long-wave shoaling (Green's law) is only 1.6 for this site (for a water depth decreasing from 39 m just outside to 20 m just inside the bay); hence, resonance must be occurring within the bay, causing the additional amplification of incoming tsunami waves. In general, a marked resonance can only occur in a semi-enclosed bay when both the wave signal is long-lasting (i.e., persistent; Ioualalen et al. 2017) and the length of the bay from its mouth to its back is an integer multiple of the quarter wavelength of dominant waves. [Persistence is required to allow for the resonance mechanism to overcome damping due to bottom friction.] Looking at Fig. 19, it appears that the dominant tsunami period is about 500 s (or 8 min) at this site; using the linear long-wave celerity for a 20-m depth, this yields a quarter wavelength of 1750 m, which is about the cross-shore length of the shallow part of the Bay (see Fig. 12); this indicates that resonance is a likely mechanism.

Wave energy spectra are shown in Fig. 20 for the time series of Fig. 19, which confirm the dominant 8-min period for each source, with a secondary dominant period around 11 min (particularly for source S11). In addition to a strong amplification of tsunami wave energy from outside to inside the bay at the 8-min period, the energy spectra show that waves are also amplified at shorter periods of 4 and 5.5 min. Hence, some resonance (albeit smaller) also occurs in the bay at these periods, which is likely in the alongshore direction, in between the two sides of the bay. In this case, resonance occurs when the bay width is a multiple of the half wavelength which, for a 240-s (4-min) period, is 1680 m, i.e., almost exactly the width of the bay at its mouth.

The occurrence of such resonances implies that should more complex fault failure scenarios occur, e.g., involving several segments rupturing over a significant time,

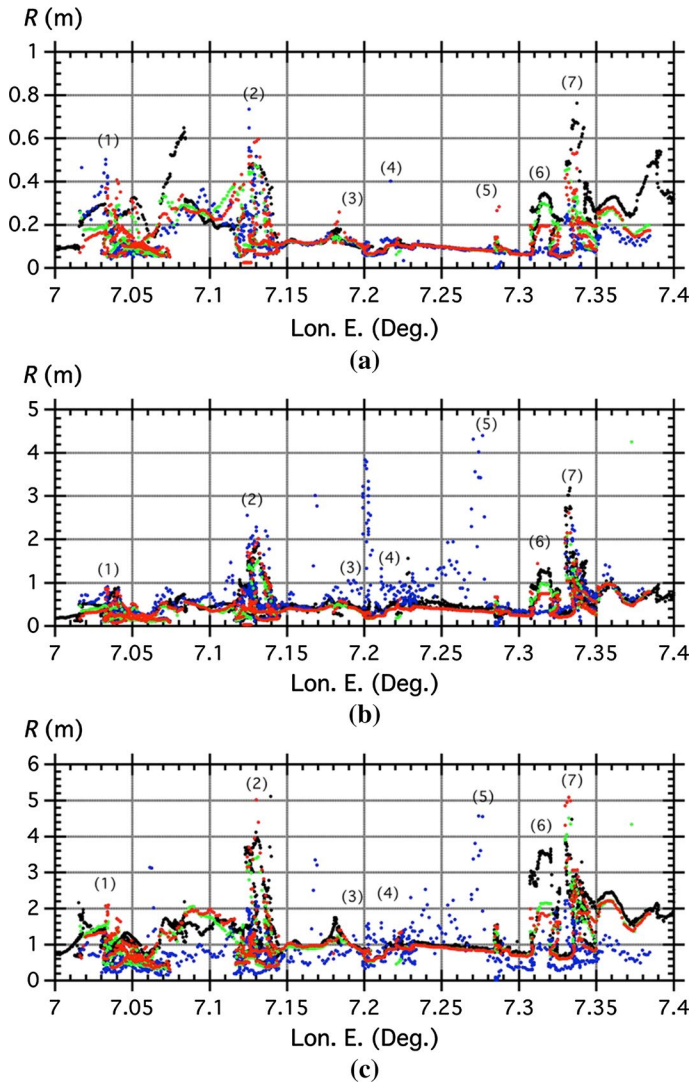


Fig. 18 Maximum runup computed along the French Riviera coast: with FUNWAVE by Ioualalen et al. (2014), in a (blue circle) 100, or (black circle) 40-m grid; and with FUNWAVE-TVD in the present study, in (green circle) 40- or (orange circle) 10-m nested grids (Table 3), for sources: **a** S7, **b** S8, **c** S11. Numbers in parenthesis mark key sites (see Figs. 3, 4): (1) Iles de Lérin (island offshore Cannes), (2) Cap d’Antibes/plage de la Salis, (3) Saint-Laurent-du-Var, (4) Nice International airport, (5) Nice-Massena (Nice harbor area), (6) Villefranche-sur-Mer, and (7) Saint-Jean Cap Ferrat

longer-lasting wave trains might be generated that could cause much larger resonances in semi-enclosed bays, such as at site 2 and at a few others sites along the French Riviera.

Table 5 Source S7. Mean and standard deviation (STD) of runups simulated in different resolution grids using FUNWAVE-TVD or FUNWAVE (Fig. 18; 850 runup points). Other basic statistics compare results in different grids, with those of FUNWAVE-TVD in the 10-m resolution grid: (RMSD) root mean square difference, (R^2) determination coefficient, L^2 norm, and (Corr) cross-correlation coefficient

S7	FUNWAVE-TVD 10 m	FUNWAVE-TVD 40 m	FUNWAVE 40 m	FUN- WAVE 100 m
Mean (m)	0.16	0.15	0.19	0.13
STD (m)	0.10	0.09	0.13	0.09
RMSD (%)		0.04	0.10	0.08
R^2		0.81	−0.03	0.27
L^2		0.23	0.53	0.45
Corr		0.90	0.70	0.65

Table 6 Same as Table 5 for source S8

S8	FUNWAVE-TVD 10 m	FUNWAVE-TVD 40 m	FUNWAVE 40 m	FUNWAVE 100 m
Mean (m)	0.46	0.43	0.51	0.71
STD (m)	0.32	0.32	0.35	0.62
RMSD (%)		0.18	0.19	0.64
R^2		0.68	0.65	−2.93
L^2		0.33	0.34	1.14
Corr		0.84	0.85	0.37

Table 7 Same as Table 5 for source S11

S11	FUNWAVE-TVD 10 m	FUNWAVE-TVD 40 m	FUNWAVE 40 m	FUNWAVE 100 m
Mean (m)	1.17	1.10	1.28	0.81
STD (m)	0.71	0.65	0.74	0.54
RMSD (%)		0.25	0.40	0.78
R^2		0.88	0.67	−0.02
L^2		0.18	0.30	0.58
Corr		0.94	0.86	0.39

3.4 Tsunami-induced currents

Another important aspect of tsunami coastal hazard, which could be more damaging to boats and facilities in small harbors and marinas than a moderate inundation, is the maximum current velocity during tsunami impact. Beyond 2–3 knots (1–1.5 m/s), such currents, which are nearly uniform over depth cause large drag forces, making navigation in and out of harbors hazardous, and starting to cause significant structural damage to harbor facilities. Additionally, large currents cause sediment scouring and deposition, which in the best-case scenario may require dredging and in the worst case can lead to

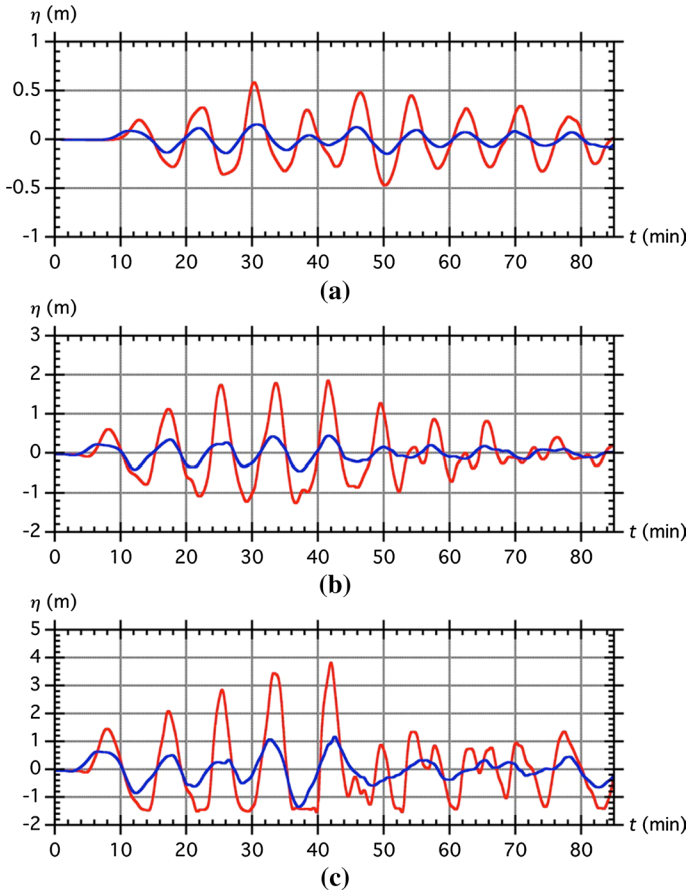


Fig. 19 Time series of surface elevations computed at Cap d’Antibes-Antibes-la Salis beach (site 2; Table 3, Fig. 4), for tsunami sources: **a** S7, **b** S8, **c** S11. In each case, wave gage stations were located within (red line) (station 8, Fig. 4) and just outside (blue line) the bay (station 9, Fig. 4)

the undermining of coastal structures such as breakwaters and seawalls (Wilson et al. 2012). Both of these effects of tsunami currents occurred during the far-field impact of the Tohoku 2011 tsunami in Crescent City harbor, CA, in which current velocity reached 7 m/s, causing over \$10 M damage to boats and harbor facilities, despite a fairly moderate tsunami inundation (Wilson et al. 2011, 2012). Observations made during the Tohoku 2011 tsunami impact in California also showed that damaging currents lasted for a much longer time than peak surface elevations (Wilson et al. 2013).

Maps of maximum simulated current velocity are plotted in Fig. 21 for tsunami source S11, for a number of channels, Bays, and small harbors/marinas along the Riviera, at and near some of the selected critical sites. The largest velocities, up to 2.5 m/s (5 knots) and larger, are predicted in Fig. 21f, h, in and around harbors/marinas located in Beaulieu-sur-Mer north of site 7 (St Jean Cap Ferrat; Table 3, Fig. 4). Large velocities (up to 3 knots) are shown in Fig. 21a, b, in the channel in between Iles de Lérin and Port Palm Beach, as well as within the harbor. As expected from the observed resonance, large velocities (up to 3 knots) also occur within the Bay of Antibes and west of it (Fig. 21c). Flow velocities are

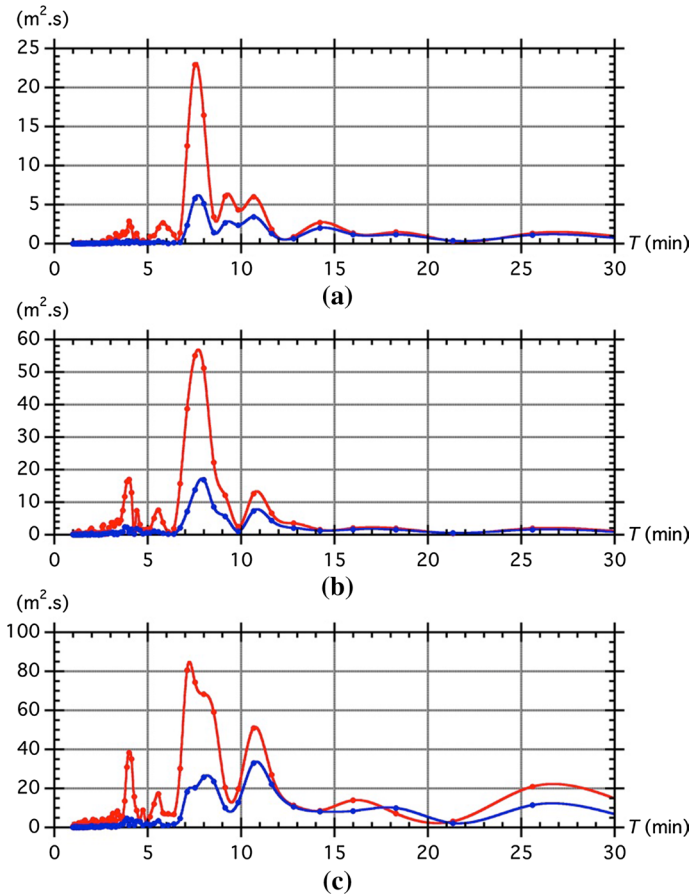


Fig. 20 Wave energy density spectra ($\text{m}^2 \cdot \text{s}$) computed as a function of wave period T for time series computed at the Cap d'Antibes-Antibes-la Salis beach gages (site 2; Table 3, Fig. 4), shown in Fig. 19, corresponding to tsunami sources: **a** S7, **b** S8, **c** S11

not large within Nice harbor (Fig. 21d), which is good as this is a fairly significant harbor in the area, but velocities are large (up to 3 knots) within the Bay of Villefranche and in the marina on its western side (Fig. 21e).

4 Discussion

The French Riviera is a seismically active area where tsunamis have frequently been triggered. The largest recorded earthquake occurred in this area on February 23, 1887, with a M_w 6.7–6.9. During this event, the eastern 30–40 km of the approximately 80-km-long Ligurian fault ruptured offshore Imperia, Italy (Larroque et al. 2012, Ioualalen et al. 2014). Events of this magnitude or possibly larger are likely to occur in the future in this area, possibly through the rupturing of the western residual 30–40-km segment of the Ligurian fault. Ioualalen et al. (2014) showed that the rupture of the entire fault system could generate a M_w 7.5 magnitude extreme event and modeled the potential tsunami coastal

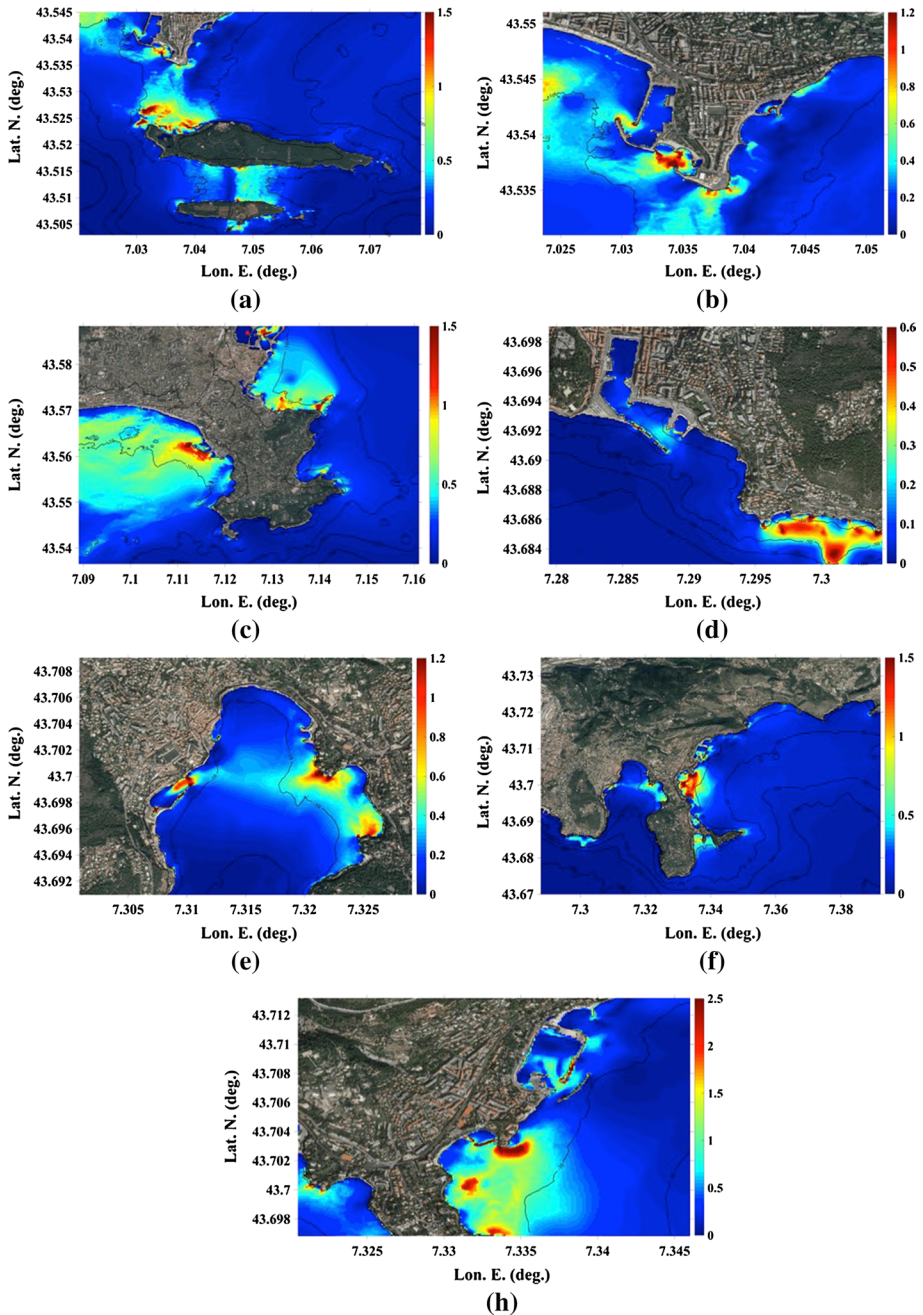


Fig. 21 Envelope of maximum current velocity (color scale in m/s), computed for source S11 in grids G3a, b, at: **a** site 1; **b** Port Palm Beach N of site 1; **c** site 2; **d** site 5; **e** site 6; **f** site 7; **h** Beaulieu-sur-Mer N of site 7 (see Table 3 and Fig. 4 for site locations)

hazard expected for this and several other earthquakes scenarios. Such modeling is typically strongly affected by uncertainties associated with the resolution of bathymetric and topographic data, particularly nearshore and onshore, as well as model grid resolution. Hence, using accurate bathymetry/topography data and high enough resolution grids is crucial, especially for complex shorelines, such as the French Riviera, where the geometry and bathymetry of small bays and harbors/marinas must be closely reproduced, to allow for tsunami-induced resonances to occur in results (as these are functions of geometry). In this respect, the US NTHMP recommends that, to perform tsunami inundation mapping, at least 10-m resolution digital elevation maps (DEMs) should be used in combination with at least 30-m, and preferably 10-m, resolution model grids. When using a dispersive wave model, such as FUNWAVE-TVD, it is also crucial to use high enough resolution model grids for the proper simulation of frequency dispersion effects in incident waves (when present). Again this requires using at least 10-m resolution coastal grids (Schambach et al. 2018). Otherwise, the model may not properly simulate constructive/destructive wave interferences, the occurrence of nearshore undular bores, and underpredict onshore inundation in some cases (Schambach et al. 2018; Glimsdal et al. 2013).

The availability of high-resolution DEMs depends on bathymetry/topography survey data that are available at the time simulations are performed. The grid resolution that is achievable in a model, while having to be commensurate with the DEM resolution, also depends in part on computational resources available. At the time of their study, unlike in the present study, Ioualalen et al. (2014) only had coarse bathymetry/topography data available for the region and they used the earlier FUNWAVE version that, although parallelized, did not allow for nested grids; hence, with the computer resources available at the time, they were limited to a relatively coarse 100-m grid resolution. While it was adequate in deeper water offshore, this resolution was too coarse along the coast to accurately simulate tsunami coastal inundation and runup, as evidenced by the present study (e.g., Fig. 18). Some harbors, such as Nice's, were clearly under-resolved: the width of the harbor entrance for instance was only represented by one or two grid points, leading to an unrealistic wave buildup, that artificially amplified wave height, causing a 28-m spurious runup value. In contrast, using a coarse grid could also cause blockage, preventing waves to enter a harbor and limiting the maximum wave height and inundation.

The newer version of the model used in this work, FUNWAVE-TVD, allows for nested grids and thus to efficiently perform simulations in high-resolution nearshore grids (here 10 m). It also allows using spherical coordinate grids, which is important at regional scales. Nevertheless, a new simulation performed here with FUNWAVE, for convergence verification and model comparison purposes, using a large single 40-m resolution grid, showed that, given a nearly adequate resolution, the predicted runups were in good agreement with those of FUNWAVE-TVD, at most locations (see Fig. 18 and Tables 5, 6, and 7). However, these simulations with FUNWAVE took several weeks to run on a large computer cluster, whereas the nested grid simulations performed with FUNWAVE-TVD only took a few hours CPUs to run each grid on a moderate-size 24-core desktop computer.

5 Conclusions

In this work, numerical simulations were performed to assess coastal tsunami hazard for three earthquake scenarios in the Ligurian Sea (M_w 6.9 or 7.5), in terms of maximum inundation, runup, and current velocity, along a large section of the French and Italian Riviera. One of the scenarios represented the M_w 6.9 1887 Ligurian event, while the M_w 7.5 scenario was a hypothetical extreme rupture mobilizing the entire Ligurian fault system. The work focused on the densely populated and highly developed coastline from Marseille, France, on the west in the Gulf of Lion, to Piombino, Italy (south of Livorno), in the Gulf of Genoa. Simulations were performed using the most recent version of FUNWAVE-TVD, a fully nonlinear and dispersive Boussinesq wave model, which features recent improvements such as: Cartesian or spherical (with Coriolis effects) coordinate grids, a better representation of friction and energy dissipation by breaking, and an improved moving shoreline algorithm. Additionally, and importantly, to alleviate problems identified in the earlier study of Ioualalen et al. (2014), as discussed above, nested grids were used (with one-way coupling), which allowed efficiently performing simulations in grids of increasing resolution toward shore: here from 640-m resolution offshore to 10-m resolution in coastal areas. Finally, a 10-m resolution DEM based on new high-resolution bathymetric data from multibeam surveys, and topographic data from coastal LIDAR surveys, was used to define grid data, including over the continental shelf (at least on the French side of the *Riviera*).

Based on this methodology, tsunami inundation maps were developed for the French side of the *Riviera*, which provide high levels of detail for assessing tsunami coastal hazard and performing future studies of coastal vulnerability and resilience. These maps can also be used to prepare for an emergency response to future local earthquakes and tsunamis. Maps reveal a large degree of spatial variability of coastal inundation and runup, depending on local effects. In general, the most impacted areas are bays, due to wave shoaling within semi-enclosed shallow areas enhanced by possible resonances. Such nearshore amplification effects are generic, i.e., they would occur for any tsunami, independent of earthquake magnitude, usually in relation to bathymetric control (i.e., causing wave convergence/divergence) and coastline geometry (i.e., causing potential resonance).

Inundation maps identified particularly vulnerable areas that should be considered as higher priority in prevention plans such as: (1) capes (*Cap d'Antibes* and *Cap Ferrat*) where wave amplification always occurs due to energy focusing; (2) semi-enclosed bays, such as *La Salis* beach at Antibes, where a wave amplification (and thus larger inundation) occurs due to resonances; (3) other small bays and marinas such as the harbor of Beaulieu-sur-Mer, which may experience strong wave-induced currents that could damage marine infrastructures and moored ships, and impede navigation, even if they are associated with only a small elevation inundation. In contrast, widely open bays, such as *Baie des Anges*, off of the major city of Nice and *Bay of Cannes* face a lesser tsunami threat due to energy defocusing. These two sites are the most densely populated urban areas of the region, especially during the summer season. It should be noted that uniform fault slip was used in the three rupture scenarios, and runup could locally be enhanced in case of more complex ruptures, such as segmented and heterogeneous ruptures.

Based on results, it appears that, even for the extreme source, a significant part of the French Riviera would not require specific emergency preparedness for co-seismic tsunamis originated in the Ligurian fault system. However, other areas identified above should be the object of further mitigation and preparedness studies. This important conclusion means

that future efforts in this respect can focus on the more exposed areas, which are of limited extent (i.e., small bays and marinas).

Acknowledgments Fatima Nemati and Stephan Grilli acknowledge support for this work from the US National Science Foundation Grant CMMI-15-35568. Mansour Ioualalen and colleagues from Géoazur acknowledge support from: (1) the European Commission under the project “Assessment, Strategy And Risk Reduction for Tsunamis in Europe,” ASTARTE (Grant No. 603839), and (2) the French government, through the UCA-JEDI Investments managed by the French National Research Agency (ANR-15-IDEX-01).

References

- Alasset PJ, Hébert H, Maoche S, Calbini V, Meghraoui M (2006) The tsunami induced by the 2003 Zemmouri earthquake ($M_w = 6.9$, Algeria): modelling and results. *Geophys J Int* 166(1):213–226
- Ambraseys NN (1960) The seismic sea wave of July 9, 1956 in the Greek archipelago. *J Geophys Res* 65:1257–1265
- Assier-Rzadkiewicz S, Heinrich P, Sabatier PC, Savoye B, Bourillet JF (2000) Numerical modeling of a landslide-generated tsunami: the 1979 Nice event. *Pure appl Geophys* 157:1707–1727
- Béthoux N, Fréchet J, Guyoton F, Thouvenot F, Cattaneo F, Nicolas M, Granet M (1992) A closing Ligurian sea. *Pure appl Geophys* 139:179–194
- Day SJ, Watts P, Grilli ST, Kirby JT (2005) Mechanical models of the 1975 Kalapana, Hawaii earthquake and tsunami. *Mar Geol* 215(1–2):59–92. <https://doi.org/10.1016/j.margeo.2004.11.008>
- Denza PF (1887) Osservazioni fatte all'Osservatorio di Moncalieri sul terremoto del 23 Febbraio 1887. *Bollettino Mensuale dell'Osservatorio Centrale Moncalieri* 2(7):68–70
- Eva C, Rabinovich AB (1997) The February 23, 1887 tsunami recorded on the Ligurian coast, western Mediterranean. *Geophys Res Lett* 24:2211–2214
- Eva E, Solarino S, Spallarossa D (2001) Seismicity and crustal structure beneath the western Ligurian Sea derived from local earthquake tomography. *Tectonophysics* 339:495–510. [https://doi.org/10.1016/S0040-1951\(01\)00106-8](https://doi.org/10.1016/S0040-1951(01)00106-8)
- Ferrari G (1991) The 1887 Ligurian earthquake: a detailed study from contemporary scientific observations. *Tectonophysics* 193:131–139
- Glimsdal S, Pedersen GK, Harbitz CB, Løvholt F (2013) Dispersion of tsunamis: does it really matter? *Nat Hazards Earth Syst Sci* 13:1507–1526. <https://doi.org/10.5194/nhess-13-1507-2013>
- Grilli S, Ioualalen M, Asavanant J, Shi F, Kirby JT, Watts P (2007) Source constraints and model simulation of the December 26, 2004 Indian Ocean tsunami. *J Waterway Port Coast Ocean Eng* 133(6):414–428. [https://doi.org/10.1061/\(ASCE\)0733-950X\(2007\)](https://doi.org/10.1061/(ASCE)0733-950X(2007))
- Grilli ST, Dubosq S, Pophet N, Pérignon Y, Kirby JT, Shi F (2010) Numerical simulation and first-order hazard analysis of large co-seismic tsunamis generated in the Puerto Rico trench: near-field impact on the North shore of Puerto Rico and far-field impact on the US East Coast. *Nat Hazards Earth Syst Sci* 10:2109–2125. <https://doi.org/10.5194/nhess-2109-2010>
- Grilli ST, Harris JC, Tajalibakhsh T, Masterlark TL, Kyriakopoulos C, Kirby JT, Shi F (2013) Numerical simulation of the 2011 Tohoku tsunami based on a new transient FEM co-seismic source: comparison to far- and near-field observations. *Pure appl Geophys* 170:1333–1359. <https://doi.org/10.1007/s00024-012-0528-y>
- Grilli ST, O'Reilly C, Harris JC, Tajalibakhsh T, Tehranirad B, Banihashemi S, Kirby JT, Baxter CDP, Eggeling T, Ma G, Shi F (2015) Modeling of SMF tsunami hazard along the upper US East Coast: detailed impact around Ocean City, MD. *Nat Hazards* 76(2):705–746. <https://doi.org/10.1007/s11069-014-1522-8>
- Grilli ST, Grilli AR, David E, Coulet C (2016) Tsunami hazard assessment along the north shore of Hispaniola from far- and near-field Atlantic sources. *Nat Hazards* 82(2):777–810. <https://doi.org/10.1007/s11069-016-2218-z>
- Grilli ST, Shelby M, Kimmoun O, Dupont G, Nicolsky D, Ma G, Kirby J, Shi F (2017) Modeling coastal tsunami hazard from submarine mass failures: effect of slide rheology, experimental validation, and case studies off the US East coast. *Nat Hazards* 86(1):353–391. <https://doi.org/10.1007/s11069-016-2692-3>
- Heidarzadeh M, Satake K (2013) The 21 May 2003 tsunami in the Western Mediterranean Sea: statistical and wavelet analyses. *Pure appl Geophys* 170(9):1449–1462
- Heidarzadeh M, Necmioglu O, Ishibe T, Yalciner AC (2017) Bodrum-Kos (Turkey-Greece) M_w 6.6 earthquake and tsunami of 20 July 2017: a test for the Mediterranean tsunami warning system. *Geosci Lett* 4:31. <https://doi.org/10.1186/s40562-017-0097-0>

- Ioualalen M, Asavanant J, Kaewbanjak N, Grilli ST, Kirby JT, Watts P (2007) Modeling of the 26th December 2004 Indian Ocean tsunami: case study of impact in Thailand. *J Geophys Res, Oceans* 112:C07024. <https://doi.org/10.1029/2006JC003850>
- Ioualalen M, Migeon S, Sardou O (2010) Landslide tsunami vulnerability in the Ligurian Sea: case study of the 1979 October 16 Nice international airport submarine landslide and of identified geological mass failures. *Geophys J Int* 181:724–740. <https://doi.org/10.1111/j.1365-246X.2010.04572.x>
- Ioualalen M, Larroque C, Scotti O, Daubord C (2014) Tsunami mapping related to local earthquakes on the French-Italian Riviera (western Mediterranean). *Pure appl Geophys* 171(7):1423–1443. <https://doi.org/10.1007/s00024-013-0699-1>
- Ioualalen M, Pelletier B, Solis Gordillo GX (2017) Investigating the March 28th 1875 and the September 20th 1920 earthquakes/tsunamis of the Southern Vanuatu arc, offshore Loyalty Islands, New Caledonia. *Tectonophysics*. <https://doi.org/10.1016/j.tecto.2017.05.006>
- Kirby JT, Shi F, Tehranirad B, Harris JC, Grilli ST (2013) Dispersive tsunami waves in the ocean: model equations and sensitivity to dispersion and Coriolis effects. *Ocean Model* 62:39–55. <https://doi.org/10.1016/j.ocemod.2012.11.009>
- Labbé M, Donnadiou C, Daubord C, Hebert H (2012) Refined numerical modeling of the 1979 tsunami in Nice (French Riviera): comparison with coastal data. *J Geophys Res* 117:F01008. <https://doi.org/10.1029/2011JF001964>
- Lambert J, Terrier M (2011) Historical tsunami database for France and its overseas territories. *Nat Hazards Earth Syst Sci* 11:1037–1046
- Larroque C, Béthoux N, Calais E, Courboux F, Deschamps A, Deverchère J, Stéphan JF, Ritz JF, Gilli E (2001) Active and recent deformation at the Southern Alps-Ligurian basin junction. *Neth J Geosci Geologie en Mijnbouw* 80:255–272
- Larroque C, Delouis B, Godel B, Nocquet J-M (2009) Active deformation at the southwestern Alps-Ligurian basin junction (France-Italy boundary): evidence for recent change from compression to extension in the Argentera massif. *Tectonophysics* 467:1–4. <https://doi.org/10.1016/j.tecto.2008.12.013>
- Larroque C, Scotti O, Ioualalen M (2012) Reappraisal of the 1887 Ligurian earthquake (western Mediterranean) from macroseismicity, active tectonics and tsunami modelling. *J. Int, Geophys*. <https://doi.org/10.1111/j.1365-246X.2012.05498.x>
- Madsen PA, Fuhrman DR, Schaffer HA (2008) On the solitary wave paradigm for tsunamis. *J Geophys Res* 113(C12012):22. <https://doi.org/10.1029/2008JC004932>
- Mård Karlsson J, Skelton A, Sanden M, Ioualalen M, Kaewbanjak N, Pophet N, von Matern A (2009) Reconstructions of the coastal impact of the 2004 Indian Ocean tsunami in the Khao Lak area, Thailand. *J Geophys Res: Oceans* 114(C10023):1–14
- Mulder T, Savoye B, Syvitsky JPM (1997) Numerical modeling of a mid-sized gravity flow: the 1979 Nice turbidity current (dynamics, processes, sediment budget and seafloor impact). *Sedimentology* 44:326–395
- Okada Y (1985) Surface deformation due to shear and tensile faults in a half-space. *Bull Seismol Soc Am* 75(4):1135–1154
- Papadopoulos GA (2015) *Tsunamis in the European-Mediterranean region: from historical record to risk mitigation*. Elsevier, Amsterdam. ISBN 978-0-12-420224-5
- Piper DJ, Savoye B (1993) Processes of late quaternary turbidity current flow and deposition on the Var deep-sea fan, north-west Mediterranean Sea. *Sedimentology* 40(3):557–582
- Schambach L, Grilli ST, Kirby JT, Shi F (2018) Landslide tsunami hazard along the upper US East Coast: effects of slide rheology, bottom friction, and frequency dispersion. *Pure Appl Geophys*. <https://doi.org/10.1007/s00024-018-1978-7>. Published online 03 Sept 2018
- Shelby M, Grilli ST, Grilli AR (2016) Tsunami hazard assessment in the Hudson River Estuary based on dynamic tsunami tide simulations. *Pure Appl Geophys* 173(12):3999–4037. <https://doi.org/10.1007/s00024-016-1315-y>
- Shi F, Kirby JT, Harris JC, Grilli ST (2012) A high order adaptive time-stepping TVD for Boussinesq modeling of breaking waves and coastal inundation. *Ocean Model* 43:36–51. <https://doi.org/10.1016/j.ocemod.2011.12.004>
- Tappin DR, Watts P, Grilli ST (2008) The Papua New Guinea tsunami of 17 July 1998: anatomy of catastrophic event. *Nat Hazards Earth Syst Sci* 8(2):243–266. <https://doi.org/www.nat-hazards-earth-syst-sci.net/8/243/2008/>
- Tappin DR, Grilli ST, Harris JC, Geller RJ, Masterlark T, Kirby JT, Shi F (2014) Did a submarine landslide contribute to the 2011 Tohoku tsunami? *Mar Geol* 357:344–361. <https://doi.org/10.1016/j.margeo.2014.09.0>
- Taramelli T, Mercalli G (1888) Il terremoto ligure del 23 febbraio 1887. *Annali dell'Ufficio Centrale Meteorologico e Geodinamico Italiano*, II 8(4):331–626

- Tehraniad B, Shi F, Kirby JT, Harris JC, Grilli ST (2011) Tsunami benchmark results for fully nonlinear Boussinesq wave model FUNWAVE-TVD. Version 1.0. Technical report, No. CACR-11-02, Center for Applied Coastal Research, University of Delaware
- Tehraniad B, Harris JC, Grilli AR, Grilli ST, Abadie S, Kirby JT, Shi F (2015) Far-field tsunami impact in the north Atlantic basin from large scale flank collapses of the Cumbre Vieja volcano, La Palma. *Pure appl Geophys* 172(12):3589–3616. <https://doi.org/10.1007/s00024-015-1135-5>
- Tinti S, Maramai A, Graziani L (2004) The new catalogue of Italian tsunamis. *Nat Hazards* 33:439–465
- Watts P, Grilli ST, Kirby JT, Fryer GJ, Tappin DR (2003) Landslide tsunami case studies using Boussinesq model and a fully nonlinear tsunami generation model. *Nat Hazards Earth Syst Sci* 3:391–402
- Wei G, Kirby JT (1995) A time-dependent numerical code for extended Boussinesq equations. *J Waterway Port Coast Ocean Eng* 121:251–261
- Wei G, Kirby JT, Grilli ST, Subramanya R (1995) A fully nonlinear Boussinesq model for surface waves. Part 1. Highly nonlinear unsteady waves. *J Fluid Mech* 294:71–92
- Wells DL, Coppersmith KJ (1994) New empirical relationships among magnitude, rupture length, rupture width, rupture area, and surface displacement. *Bull Seismol Soc Am* 84(4):974–1002
- Wilson R, Dengler L, Borrero J, Synolakis C, Jaffe B, Barberopoulou A, Ewing L, Legg M, Ritchie A, Lynett P, Admire A, McCrink T, Falls J, Rosinski A, Treiman J, Manson M, Silva M, Davenport C, Lancaster J, Olson B, Pridmore C, Real C, Miller K, Goltz J (2011) The effects of the 2011 Tohoku tsunami on the California coastline. *Seismol Res Lett* 82(3):459–460
- Wilson R, Davenport C, Jaffe B (2012) Sediment scour and deposition within harbors in California (USA), caused by the March 11, 2011 Tohoku-oki Tsunami. *Sed Geol* 282:228–240
- Wilson RI, Admire AR, Borrero JC, Dengler LA, Legg MR, Lynett P, Mc Crink TP, Miller KM, Ritchie A, Sterling K, Whitmore PM (2013) Observations and Impacts from the 2010 Chilean and 2011 Japanese Tsunamis in California (USA). *Pure appl Geophys* 170(6–8):1127–1147. <https://doi.org/10.1007/s00024-012-0527-z>

Publisher's Note Springer Nature remains neutral with regard to jurisdictional claims in published maps and institutional affiliations.